



Cam-Clay plasticity, Part VIII: A constitutive framework for porous materials with evolving internal structure

Ronaldo I. Borja*, Jinhyun Choo

Department of Civil and Environmental Engineering, Stanford University, Stanford, CA 94305, USA

Received 7 January 2016; received in revised form 12 June 2016; accepted 14 June 2016

Available online 29 June 2016

Abstract

Natural geomaterials often exhibit pore size distributions with two dominant porosity scales. Examples include fractured rocks where the dominant porosities are those of the fractures and rock matrix, and aggregated soils where the dominant porosities are those of the micropores and macropores. We develop a constitutive framework for this type of materials that covers both steady-state and transient fluid flow responses. The framework relies on a thermodynamically consistent effective stress previously developed for porous media with two dominant porosity scales. We show that this effective stress is equivalent to the weighted sum of the individual effective stresses in the micropores and macropores, with the weighting done according to the pore fractions. This partitioning of the effective stress into two single-porosity effective stresses allows fluid pressure dissipation at the macropores and micropores to be considered separately, with important implications for individual characterization of the hardening responses at the two pore scales. Experimental data suggest that the constitutive framework captures the laboratory responses of aggregated soils more accurately than other models previously reported in the literature. Numerical simulations of boundary-value problems reveal the capability of the framework to capture the effect of secondary compression as the micropores discharge fluids into the macropores.

© 2016 Elsevier B.V. All rights reserved.

Keywords: Coupled problem; Double porosity; Effective stress; Mixture theory

1. Introduction

Many natural geomaterials such as aggregated soils and fissured rocks exhibit pore size distributions with two dominant values of porosity [1–6]. In fissured rocks the two scales of porosity are those of the rock matrix and fractures [7–15], whereas in aggregated soils, the two scales of porosity pertain to those of the micropores (intra-aggregate pores) and macropores (inter-aggregate pores), which can be filled up with one or more types of fluid [16–23]. Of interest in these so-called ‘double-porosity’ media is the evolution of the internal structure and the proportional changes in the micro- and macro-porosities during the course of loading [24–28]. Using a combination of tomography techniques and image analysis on aggregated soils, Koliji et al. [29] showed that the volume and structure of the macropores are

* Corresponding author.

E-mail address: borja@stanford.edu (R.I. Borja).

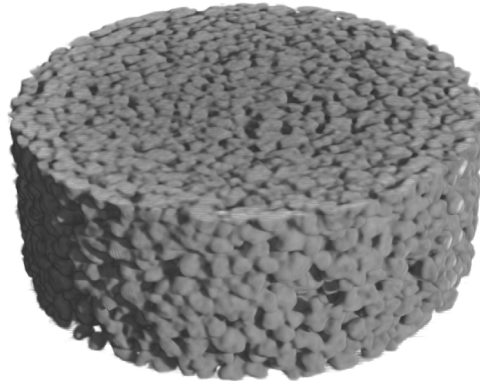


Fig. 1. Reconstructed computed tomography volume of an aggregated silty clay, diameter = 80 mm, height = 35 mm. The aggregates are composed of much smaller silty clay solid particles with intra-aggregate pores. Visible spaces between aggregates are the inter-aggregate pores. After Koliji [30] and Borja and Koliji [46].

strongly affected by the mechanical loading, while the corresponding changes in the micropores are almost insignificant. They showed that significant changes in the structure occurs with plastic straining, leading to an evolution law that links the macroporosity alteration to plastic strain [30,31].

Early applications of double-porosity concepts have focused on the behavior of fissured rocks with respect to their ability to transmit fluid through the matrix pores and fractures [32,33]. Subsequent developments have addressed fluid flow through aggregated soils and their implications for the so-called ‘effective stress’ in materials with double porosity [34–37]. Many of the proposed expressions for the effective stress in two-porosity fields lacked a thermodynamic basis that has been the cornerstone of similar developments for single-porosity problems [38–45]. An exception is the expression for the effective stress in two-porosity fields developed by Borja and Koliji [46], which emanated directly from mixture theory and continuum principles of thermodynamics. Despite these efforts to develop a suitable measure of effective stress, however, much work remains to be done with respect to mathematically delineating the evolution of internal structure and how it impacts fluid flow through the micropores and macropores of materials with two dominant porosity scales.

This work focuses more specifically on the behavior of aggregated soils depicted by the computed tomography volume of Fig. 1. The volume contains aggregates of reconstituted soil with much smaller intra-aggregate pores (micropores), as compared to the much larger inter-aggregate pores (macropores) that are very visible in the figure. For the sake of clarity, we use the concept of ‘dual permeability’ in which fluid may flow not only through the larger macropores but also through the smaller micropores, as well as between contacting aggregates through their contact areas [47,48]. Fluid may also be exchanged between the micropores and macropores through the surface of the aggregates exposed to the inter-aggregate pores [49]. The macropores define the internal structure of the volume. As the volume is compressed both the macropores and micropores can compact, but the compaction of the macropores is more dominant during the early stages of compression. As the macropores are squeezed the internal structure disappears [50], leaving behind a volume with only the micropores and having a similar material behavior to that of the reconstituted soil.

A challenge with modeling double-porosity media is that there are two compressibility responses that must be captured within the same constitutive framework—that of the reconstituted material with an evolving internal structure, and that of the reconstituted material itself [51,25,26]. Because the internal structure disappears with collapse of the macropores, the response of the system with internal structure must necessarily approach the response of the reconstituted material itself at high compressive loads. This requires a nonlinear continuum mechanics approach accommodating an evolving configuration in general and an evolving macro-porosity in particular. If the macropores and micropores are filled with fluids that are free to migrate within and outside their pore scales, then the constitutive framework must also accommodate two volume constraints imposed by the two pore scales. Furthermore, in the context of critical state theory [52,50] the preconsolidation stresses at the two pore scales must also be tracked concurrently with fluid pressure dissipation.

This paper takes a nonlinear continuum mechanics approach to accommodate an evolving internal structure by partitioning the overall effective stress of double-porosity media into two single-porosity effective stresses appropriate for the macropores and micropores. In doing so, fluid pressure dissipation at the two pore scales as well as the

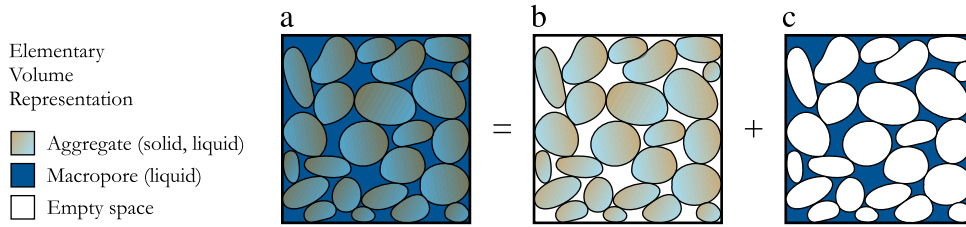


Fig. 2. Schematic representation of aggregated soil with double porosity: (a) total saturated mixture of solid and liquid; (b) aggregate of solid and liquid; and (c) macropores completely filled with liquid. After Koliji [30] and Borja and Koliji [46].

accompanying hardening of the preconsolidation stresses can be tracked individually. The core aspect of the formulation is the expression for the rate of change of internal energy for double-porosity media [46], which determines the energy-conjugate pairing of the relevant constitutive variables. The constitutive model is cast within the mixed finite element framework. Without loss of generality, we assume throughout this paper that the two pore scales are fully saturated with the same type of fluid (e.g. water), and leave the subject of partial saturation, in which the two pore scales may be filled with more than one type of fluid, for future work.

2. General formulation

This section focuses on the kinematics of deformation of a porous solid with double porosity. The general notion of compressibility in the context of double porosity is also introduced, along with a formulation of elastoplasticity in terms of the effective Kirchhoff stress that incorporates an evolving internal structure, herein represented by the pore fraction ψ .

2.1. Solid kinematics

Consider an aggregated soil with elementary volume shown schematically in Fig. 2. The motion of the solid is defined by the deformation $\mathbf{x} = \boldsymbol{\phi}(\mathbf{X}, t)$, with deformation gradient $\mathbf{F} = \partial\boldsymbol{\phi}/\partial\mathbf{X}$. The solid deformation carries with it both the macropore and micropore volumes quantified by the void ratios

$$e_m(\mathbf{X}, t) = \frac{dV_{vm}}{dV_s}, \quad e_M(\mathbf{X}, t) = \frac{dV_{vM}}{dV_s}, \tag{1}$$

where dV_{vm} and dV_{vM} are the volumes of the micropores and macropores, respectively, and dV_s is the volume of solid contained in the elementary volume. We also define the following volume fractions

$$\phi^s(\mathbf{X}, t) = \frac{dV_s}{dV}, \quad \psi(\mathbf{X}, t) = \frac{dV_{vm}}{dV_v}, \tag{2}$$

where $dV_v = dV_{vm} + dV_{vM}$ is the total volume of the void within the total volume dV of the mixture. In this last equation, ϕ^s is the solid volume fraction while ψ is the fraction of the void occupied by the micropores.

The specific volume of the micropores is given by

$$v_m(\mathbf{X}, t) = 1 + e_m(\mathbf{X}, t), \tag{3}$$

which is the total volume of the aggregate per unit solid volume. The overall specific volume is

$$v(\mathbf{X}, t) = v_m(\mathbf{X}, t) + e_M(\mathbf{X}, t), \tag{4}$$

which is the total volume of the mixture per unit solid volume. In aggregated soils, the aggregate is typically associated with a reconstituted material with no internal structure such as clay. On the other hand, the internal structure of the soil is defined by the macropores. We note that $v(\mathbf{X}, t) \rightarrow v_m(\mathbf{X}, t)$ as $e_M(\mathbf{X}, t) \rightarrow 0$, which means that the internal structure of the soil disappears when the macropores collapse.

If the solid does not exchange mass with the fluid, then its motion should be mass conserving. Dropping the spatial and temporal arguments \mathbf{X} and t for brevity, this means that

$$\overline{J\phi^s\rho_s} = 0, \tag{5}$$

where $J = \det(\mathbf{F})$ is the Jacobian of the solid motion, ρ_s is the intrinsic mass density of the solid, and the superimposed dot denotes a material time derivative with respect to the solid motion. Without loss of generality we shall assume that the solid constituent is incompressible and take $\rho_s = \text{constant}$, which yields the following evolution of the solid volume fraction

$$\dot{\phi}^s = \frac{\dot{\phi}_0^s}{J}, \quad (6)$$

where ϕ_0^s is the volume fraction of the solid when $J = J_0 = 1$. Thus, the evolution of ϕ^s can be determined from the variation of the Jacobian J alone.

The evolutions of the specific volumes are given by

$$v = \frac{1}{\phi^s} = \frac{J}{\phi_0^s} \quad (7)$$

for the macropores, and

$$v_m = 1 + \psi \frac{1 - \phi^s}{\phi^s} = 1 - \psi + \frac{\psi J}{\phi_0^s} \quad (8)$$

for the micropores. Note that the expression for v is determined by J alone, whereas the expression for v_m also contains the pore fraction ψ that must be determined separately. The difference between the two specific volumes is the void ratio of the macropores,

$$e_M = v - v_m = (1 - \psi) \frac{1 - \phi^s}{\phi^s} = (1 - \psi) \left(\frac{J}{\phi_0^s} - 1 \right). \quad (9)$$

2.2. Effective stress and the first law

For double-porosity media whose macropores (denoted by index M) and micropores (denoted by index m) are saturated with incompressible fluid (e.g. water), the rate of change of internal energy per unit volume takes the form [46,53]

$$J\rho\dot{e} = \langle \bar{\boldsymbol{\tau}}, \mathbf{d} \rangle + \sum_{i=M,m} \langle \tilde{\mathbf{v}}_i, \dot{\phi}^i, p_i \rangle - \sum_{i=M,m} \langle c^i, p_i, \tilde{\mathbf{v}}_i \rangle - \langle (1 - \phi^s), \boldsymbol{\pi}, \dot{\psi} \rangle, \quad (10)$$

where the symbol $\langle \circ, \dots, \circ \rangle$ denotes energy-conjugate pairing in product form. The notations are as follows: \dot{e} is the rate of change of internal energy per unit total mass of the mixture, ρ is the total mass density of the mixture, $\bar{\boldsymbol{\tau}}$ is the effective Kirchhoff stress tensor, \mathbf{d} is the rate of deformation tensor, $\tilde{\mathbf{v}}_i$ is the relative velocity of fluid in pore scale i with respect to solid, ϕ^i is the volume fraction of pore scale i , p_i is the intrinsic Kirchhoff fluid pressure in pore scale i , c^i is a mass exchange term satisfying the closure condition $c^M + c^m = 0$, ϕ^s is the volume fraction of solid (defined previously), ψ is the void fraction for the micropores (also defined previously), and

$$\boldsymbol{\pi} = p_M \mathbf{1} - p_m \mathbf{1} \quad (11)$$

is the Kirchhoff fluid pressure jump between the two pore scales. The Kirchhoff stresses and pressures differ from the Cauchy definitions by the factor J , i.e., $\bar{\boldsymbol{\tau}} = J\bar{\boldsymbol{\sigma}}$ and $p_i = J\theta_i$, where $\bar{\boldsymbol{\sigma}}$ is the Cauchy effective stress tensor and θ_i is the Cauchy fluid pressure in pore scale i . The foregoing expression for the rate of change of internal energy yields four groups of constitutive variables that imply four types of constitutive relations. We shall elaborate these pairs of constitutive relations in a later section, but for now we focus on the effective stress $\bar{\boldsymbol{\sigma}}$ and the fourth term in the energy equation involving the pressure jump $\boldsymbol{\pi}$.

The effective Kirchhoff stress tensor is given by the expression [46]

$$\bar{\boldsymbol{\tau}} = \boldsymbol{\tau} + \bar{p}\mathbf{1}, \quad (12)$$

where $\boldsymbol{\tau}$ is the total Kirchhoff stress tensor, $\mathbf{1}$ is the second-order identity tensor, and \bar{p} is the Kirchhoff mean fluid pressure given by

$$\bar{p} = \psi p_m + (1 - \psi)p_M. \quad (13)$$

Here, we take the Biot coefficient equal to unity following the earlier assumption of an incompressible solid constituent. Rewriting the total Kirchhoff stress tensor as $\boldsymbol{\tau} = \psi \boldsymbol{\tau} + (1 - \psi)\boldsymbol{\tau}$, we find that

$$\bar{\boldsymbol{\tau}} = \psi \bar{\boldsymbol{\tau}}_m + (1 - \psi)\bar{\boldsymbol{\tau}}_M, \tag{14}$$

where

$$\bar{\boldsymbol{\tau}}_m = \boldsymbol{\tau} + p_m \mathbf{1}, \quad \bar{\boldsymbol{\tau}}_M = \boldsymbol{\tau} + p_M \mathbf{1} \tag{15}$$

are the single-porosity effective Kirchhoff stress tensors at each pore scale [43]. Note that these two stress tensors are not independent, but instead are related by the equation

$$\bar{\boldsymbol{\tau}}_m = \bar{\boldsymbol{\tau}}_M - \pi \mathbf{1}. \tag{16}$$

In other words, the two single-porosity effective stresses are simply translated on the hydrostatic axis by the fluid pressure jump π .

We now consider an isotropic state of stress and denote the mean normal effective stresses by the symbols $\bar{\tau}_m = \text{tr}(\bar{\boldsymbol{\tau}}_m)/3$ and $\bar{\tau}_M = \text{tr}(\bar{\boldsymbol{\tau}}_M)/3$. Eq. (16) thus reduces to

$$\pi = \bar{\tau}_M - \bar{\tau}_m. \tag{17}$$

When the macropores and micropores are both yielding, the effective mean normal stresses may be replaced by their respective preconsolidation stresses, i.e., $\bar{\tau}_m = p_{cm}$ and $\bar{\tau}_M = p_{cM}$. The overall preconsolidation stress for the aggregated soil is then equal to

$$\bar{\tau} = \frac{1}{3} \text{tr}(\bar{\boldsymbol{\tau}}) = \psi \bar{\tau}_m + (1 - \psi)\bar{\tau}_M := \bar{p}_c, \tag{18}$$

where

$$\bar{p}_c = \psi p_{cm} + (1 - \psi)p_{cM}. \tag{19}$$

When the material is yielding the fluid pressure jump is also equal to the jump in the preconsolidation pressures, i.e.,

$$\pi = p_{cM} - p_{cm}. \tag{20}$$

The fourth energy-conjugate term on the right-hand side of Eq. (10) suggests compressibility laws of the form $p_{cm} = p_{cm}(\phi^s, \psi)$ and $p_{cM} = p_{cM}(\phi^s, \psi)$, which give

$$\pi = p_{cM}(\phi^s, \psi) - p_{cm}(\phi^s, \psi) \equiv g(\phi^s, \psi). \tag{21}$$

For incompressible solid constituents, variations in void fraction ϕ^s are associated with changes in the volume of the pores. If such changes are irreversible, or if the reversible component is insignificant, then compressibility laws of the following form may be used

$$\pi = \tilde{g}(J^P, \psi), \tag{22}$$

where J^P is the plastic component of J . The next section elaborates how these compressibility laws impact the evolution of the internal structure of a material with two porosity scales, as well as how they compare with other compressibility laws developed for aggregated soils such as Bioley silt [31] and Corinth marl [51].

2.3. Compressibility laws

Consider a ‘normally consolidated’ porous material where both the macropores and micropores are yielding such that the internal structure evolves according to the following compressibility laws,

$$v_m = f(p_{cm}), \quad e_M = g(p_{cM}). \tag{23}$$

The inverse relations are given by

$$p_{cm} = f^{-1}(v_m), \quad p_{cM} = g^{-1}(e_M). \tag{24}$$

Note that p_{cm} and p_{cM} vary with ϕ^s and ψ through v_m and e_M , respectively, see Eqs. (8) and (9).

Now, assume that there is no pore pressure jump between the micropores and macropores so that $\pi = 0$. This condition holds if both pore scales are dry, or if the load is applied at a sufficiently slow rate that no pore pressure difference develops between the two pore scales. Setting $p_{cm} = p_{cM} \equiv \bar{p}_c$ determines the evolution of the micropore fraction ψ for a given evolution of ϕ^s (or J). Note that the compressibility laws are generally of nonlinear form, so a closed-form expression for ψ may not be readily available. However, in principle one can always calculate ψ numerically (by iteration, for example). Having determined the variation of ψ with J , one can then substitute it back into the expression for the preconsolidation stress to obtain the corresponding variation of \bar{p}_c as a function of J . Thus, both ψ and \bar{p}_c can be determined from the given time history of J .

Now, suppose that instead of J we are given the time history of the effective isotropic stress $\bar{\tau} \equiv \bar{p}_c$, and assume once again that $\pi = 0$. The goal is to find ψ and J such that

$$p_{cm} = f^{-1}(v_m(\psi, J)) \equiv \bar{p}_c, \quad (25)$$

and

$$p_{cM} = g^{-1}(e_M(\psi, J)) \equiv \bar{p}_c. \quad (26)$$

We have two equations in two unknowns, so we can determine the variations of J and ψ from the given time history of \bar{p}_c . If $\pi \neq 0$, then its time history must be prescribed to determine the evolution of the micropore fraction ψ .

The specific compressibility laws of interest are of the following form. For the micropores, we have

$$\frac{\dot{v}_m}{v_m} = -c_c \frac{\dot{p}_{cm}}{p_{cm}}, \quad \dot{\varepsilon}_v^e = -c_r \frac{\dot{p}_{cm}}{p_{cm}}, \quad (27)$$

where c_c and c_r are total and elastic compressibility indices, respectively, and ε_v^e is the elastic logarithmic volumetric strain. Direct time integration gives

$$p_{cm} = (p_{cm})_n \exp\left[-\frac{\ln(v_m/v_{mn}) - (\varepsilon_v^e - \varepsilon_{vn}^e)}{c_c - c_r}\right], \quad (28)$$

where subscript n pertains to reference value at time t_n , and $v_m = v_m(\psi, v)$ from Eq. (8). This equation is equivalent to the bilogarithmic compressibility law proposed by Butterfield [54] for reconstituted soils.

For the macropores, we consider a similar bilogarithmic compressibility law of the form

$$\frac{\dot{e}_M}{e_M} = -c_M \frac{\dot{p}_{cM}}{p_{cM}}, \quad (29)$$

where c_M is the compressibility index determined from the macropore compressibility curve, which is the difference between the total and micropore compressibility curves. Integrating yields

$$p_{cM} = (p_{cM})_n \exp\left[-\frac{\ln(e_M/e_{Mn})}{c_M}\right]. \quad (30)$$

This law predicts an asymptotic decay in the sense $v \rightarrow v_m$ as $-p_{cM} \rightarrow \infty$. Later we shall validate these compressibility laws against experimental data on aggregated soils.

2.4. Continuum formulation

This section formulates the rate constitutive equations for double-porosity continua with an evolving internal structure represented by the scalar variable ψ . The formulation is done in abstract form to elucidate the essential ingredients of the theory. More specific elements of the theory are presented in the next section. Our point of departure is the rate constitutive equation in effective Kirchhoff stress space of the form (see equation (5.82) of [55])

$$\dot{\bar{\tau}} = \alpha^e : \left(\mathbf{d} - \dot{\lambda} \frac{\partial G}{\partial \bar{\tau}} \right), \quad (31)$$

where \mathbf{d} is the symmetric part of the velocity gradient tensor \mathbf{I} , called the rate-of-deformation tensor, G is the plastic potential function, $\dot{\lambda} \geq 0$ is the plastic consistency parameter, and α^e is a rank-four elastic tangent tensor analogous to

the elastic constitutive tensor $\boldsymbol{\alpha}^e$ in infinitesimal theory. We should note that $\boldsymbol{\alpha}^e$ is amenable to spectral decomposition (see equation (5.88) of [55]), and contains the initial stress terms necessary to make the transformation objective with respect to rigid-body rotation. Because $\bar{\boldsymbol{\tau}}$ is a symmetric tensor, the plastic flow direction $\partial G/\partial \bar{\boldsymbol{\tau}}$ is also a symmetric tensor, which means that the plastic spin is ignored.

Next, we consider a yield function of the form $F(\bar{\boldsymbol{\tau}}, \bar{p}_c) \leq 0$. Assuming the yield condition $F = 0$ is satisfied, the consistency condition for continued yielding takes the form

$$\dot{F} = 0 \quad \Rightarrow \quad \frac{\partial F}{\partial \bar{\boldsymbol{\tau}}} : \dot{\bar{\boldsymbol{\tau}}} + \frac{\partial F}{\partial \bar{p}_c} \dot{\bar{p}}_c = 0, \tag{32}$$

where

$$\dot{\bar{p}}_c = \frac{\partial \bar{p}_c}{\partial \psi} \dot{\psi} + \frac{\partial \bar{p}_c}{\partial J^p} \dot{J}^p \equiv \alpha_1 \dot{\psi} + \alpha_2 \dot{\lambda}. \tag{33}$$

In this last equation, we take $\dot{J}^p \propto \dot{\lambda}$ and α_2 is some scalar coefficient of the consistency parameter $\dot{\lambda}$.

We now eliminate $\dot{\psi}$ by appealing to Eq. (22). Taking the rates gives

$$\dot{\pi} = \frac{\partial \tilde{g}}{\partial \psi} \dot{\psi} + \frac{\partial \tilde{g}}{\partial J^p} \dot{J}^p \equiv \beta_1 \dot{\psi} + \beta_2 \dot{\lambda}. \tag{34}$$

Here, we note that $\dot{\pi}$ is a *given* function representing the rate of fluid jump between the two pore scales. Provided that $\beta_1 \neq 0$, we can solve for $\dot{\psi}$ and substitute into (33) to obtain

$$\dot{\bar{p}}_c = \frac{\alpha_1}{\beta_1} \dot{\pi} - \left(\frac{\alpha_1 \beta_2}{\beta_1} - \alpha_2 \right) \dot{\lambda}. \tag{35}$$

To determine the consistency parameter, we substitute the constitutive equation (31) and hardening law (35) into the consistency condition (32) and solve for $\dot{\lambda}$. The result reads

$$\dot{\lambda} = \frac{1}{\chi} \left(\frac{\partial F}{\partial \bar{\boldsymbol{\tau}}} : \boldsymbol{\alpha}^e : \mathbf{d} + \frac{\partial F}{\partial \bar{p}_c} \frac{\alpha_1}{\beta_1} \dot{\pi} \right), \tag{36}$$

where

$$\chi = \frac{\partial F}{\partial \bar{\boldsymbol{\tau}}} : \boldsymbol{\alpha}^e : \frac{\partial G}{\partial \bar{\boldsymbol{\tau}}} + H, \quad H = \frac{\partial F}{\partial \bar{p}_c} \left(\alpha_2 - \frac{\alpha_1 \beta_2}{\beta_1} \right). \tag{37}$$

Substituting the consistency parameter back into the constitutive equation (31) and simplifying yields

$$\dot{\bar{\boldsymbol{\tau}}} = \boldsymbol{\alpha}^{ep} : \mathbf{d} + \boldsymbol{\theta} \dot{\pi}, \tag{38}$$

where

$$\boldsymbol{\alpha}^{ep} = \boldsymbol{\alpha}^e - \frac{1}{\chi} \boldsymbol{\alpha}^e : \frac{\partial G}{\partial \bar{\boldsymbol{\tau}}} \otimes \frac{\partial F}{\partial \bar{\boldsymbol{\tau}}} : \boldsymbol{\alpha}^e \tag{39}$$

and

$$\boldsymbol{\theta} = -\frac{1}{\chi} \frac{\partial F}{\partial \bar{p}_c} \frac{\alpha_1}{\beta_1} \boldsymbol{\alpha}^e : \frac{\partial G}{\partial \bar{\boldsymbol{\tau}}}. \tag{40}$$

This result indicates that the effective Kirchhoff stress is driven not only by the solid velocity gradient but also by the fluid pressure jump between the two pore scales, which in turn arises from the difference in the preconsolidation stresses between the macropores and micropores.

3. Finite element formulation

This section presents a $\mathbf{u}/p_M/p_m$ finite element formulation for porous materials with double porosity, where \mathbf{u} = solid displacement vector, p_M = macropore fluid pressure, and p_m = micropore fluid pressure. The formulation

follows the standard lines of hydromechanical coupling [56–59,53,60–67], except that it now treats the micropore fraction ψ as an internal variable related to the independent variables by the relevant constitutive law. The section concludes with a discussion of the stress-point integration algorithm accommodating the evolution of the pore fraction in the finite deformation range.

3.1. Conservation laws and strong form

Before presenting the relevant conservation laws, we first recall some preliminary results pertinent to finite deformation analysis (see [68,69]). The first Piola–Kirchhoff stress tensor is $\mathbf{P} = \boldsymbol{\tau} \cdot \mathbf{F}^{-\text{T}}$ and the corresponding effective stress tensor is $\bar{\mathbf{P}} = \bar{\boldsymbol{\tau}} \cdot \mathbf{F}^{-\text{T}}$. The effective stress equation in terms of these stress tensors takes the form

$$\mathbf{P} = \bar{\mathbf{P}} - \bar{p}\mathbf{F}^{-\text{T}}, \quad (41)$$

where \bar{p} is the Kirchhoff mean fluid pressure defined in Eq. (13).

The total mass density is the sum of the partial mass densities,

$$\rho = \rho^s + \rho^M + \rho^m. \quad (42)$$

The partial mass densities are given by

$$\rho^s = \phi^s \rho_s, \quad \rho^M = (1 - \phi^s)(1 - \psi)\rho_w, \quad \rho^m = (1 - \phi^s)\psi\rho_w, \quad (43)$$

where the intrinsic mass densities ρ_s and ρ_w are assumed constant. The pullback mass densities are

$$\rho_0 = J\rho = \rho_0^s + \rho_0^M + \rho_0^m. \quad (44)$$

We recall that $\dot{\rho}_0^s = \dot{J}\rho^s = 0$ if the solid does not exchange mass with the fluid, see Eq. (5). Thus,

$$\dot{\rho}_0^M = \dot{J}\rho^M = (1 - \psi)\dot{J}\rho_w - J(1 - \phi^s)\dot{\psi}\rho_w, \quad (45)$$

$$\dot{\rho}_0^m = \dot{J}\rho^m = \psi\dot{J}\rho_w + J(1 - \phi^s)\dot{\psi}\rho_w. \quad (46)$$

The relative fluid velocities in the macropores and micropores are defined with respect to the solid velocity \mathbf{v} and take the form

$$\tilde{\mathbf{v}}_M = \mathbf{v}_M - \mathbf{v}, \quad \tilde{\mathbf{v}}_m = \mathbf{v}_m - \mathbf{v}, \quad (47)$$

where \mathbf{v}_M and \mathbf{v}_m are the fluid velocities in the macropores and micropores, respectively. These relative velocities give rise to fluid mass fluxes

$$\mathbf{q}_M = \rho^M \tilde{\mathbf{v}}_M, \quad \mathbf{q}_m = \rho^m \tilde{\mathbf{v}}_m, \quad (48)$$

with Piola transforms

$$\mathbf{Q}_M = J\mathbf{F}^{-1} \cdot \mathbf{q}_M, \quad \mathbf{Q}_m = J\mathbf{F}^{-1} \cdot \mathbf{q}_m. \quad (49)$$

We now consider a fluid-saturated body \mathcal{B} with boundary $\partial\mathcal{B}$ in the reference configuration, and assume that the solid matrix possesses two porosity scales. The boundary $\partial\mathcal{B}$ admits the decomposition

$$\partial\mathcal{B} = \overline{\partial\mathcal{B}_u} \cup \overline{\partial\mathcal{B}_t}, \quad \emptyset = \partial\mathcal{B}_u \cap \partial\mathcal{B}_t, \quad (50)$$

where $\partial\mathcal{B}_u$ and $\partial\mathcal{B}_t$ are Dirichlet and Neumann boundaries with displacement and tractions prescribed. For quasistatic loading the balance of linear momentum takes the form [46]

$$\text{DIV}(\mathbf{P}) + \rho_0\mathbf{G} = c_0(\tilde{\mathbf{v}}_m - \tilde{\mathbf{v}}_M) \quad \text{in } \mathcal{B}, \quad (51)$$

where DIV is the Lagrangian divergence operator, \mathbf{G} is the gravity acceleration vector, and $c_0 = Jc$ is the pullback fluid mass transfer coefficient, with c being the value in the current configuration, reflecting transfer of fluid mass into or from the micropores. The relevant boundary and initial conditions are $\mathbf{u} = \mathbf{u}^*$ on $\partial\mathcal{B}_u$, $\mathbf{P} \cdot \mathbf{N} = \mathbf{t}$ on $\partial\mathcal{B}_t$, and $\mathbf{u}(\mathbf{X}) = \mathbf{u}_0(\mathbf{X})$ at time $t = 0$ and for all $\mathbf{X} \in \mathcal{B}$.

We also consider the following decomposition of $\partial\mathcal{B}$

$$\partial\mathcal{B} = \overline{\partial\mathcal{B}_{p_M} \cup \partial\mathcal{B}_{q_M}}, \quad \emptyset = \partial\mathcal{B}_{p_M} \cap \partial\mathcal{B}_{q_M} \tag{52}$$

for the macropores, and

$$\partial\mathcal{B} = \overline{\partial\mathcal{B}_{p_m} \cup \partial\mathcal{B}_{q_m}}, \quad \emptyset = \partial\mathcal{B}_{p_m} \cap \partial\mathcal{B}_{q_m} \tag{53}$$

for the micropores, where p and q are pressure and flux boundary conditions, respectively. The fluid mass conservation equations in the macropores and micropores take the form [46]

$$\dot{\rho}_0^M + \text{DIV}(\mathbf{Q}_M) = -c_0 \quad \text{in } \mathcal{B}, \tag{54}$$

$$\dot{\rho}_0^m + \text{DIV}(\mathbf{Q}_m) = c_0 \quad \text{in } \mathcal{B}. \tag{55}$$

The boundary conditions are as follows: $p_M = p_M^*$ on $\partial\mathcal{B}_{p_M}$, $p_m = p_m^*$ on $\partial\mathcal{B}_{p_m}$, $\mathbf{Q}_M \cdot \mathbf{N} = Q_M$ on $\partial\mathcal{B}_{q_M}$, and $\mathbf{Q}_m \cdot \mathbf{N} = Q_m$ on $\partial\mathcal{B}_{q_m}$. The initial conditions are: $p_M(\mathbf{X}) = p_{M0}(\mathbf{X})$ and $p_m(\mathbf{X}) = p_{m0}(\mathbf{X})$ at time $t = 0$ and for all $\mathbf{X} \in \mathcal{B}$.

3.2. Variational equations

To develop the weak form, we need the space of configurations denoted by

$$\mathcal{U}_u = \{\mathbf{u} : \mathcal{B} \rightarrow \mathbb{R}^{n_{sd}} | u_i \in H^1, \mathbf{u} = \mathbf{u}^* \text{ on } \partial\mathcal{B}_u\}, \tag{56}$$

and the space of variations

$$\mathcal{V}_u = \{\boldsymbol{\eta} : \mathcal{B} \rightarrow \mathbb{R}^{n_{sd}} | \eta_i \in H^1, \boldsymbol{\eta} = \mathbf{0} \text{ on } \partial\mathcal{B}_u\}, \tag{57}$$

where H^1 is the Sobolev space of functions of degree one. The variational form of linear momentum balance is given by

$$\int_{\mathcal{B}} \left(\text{GRAD } \boldsymbol{\eta} : \mathbf{P} - \rho_0 \boldsymbol{\eta} \cdot \mathbf{G} + c_0(\tilde{\mathbf{v}}_m - \tilde{\mathbf{v}}_M) \right) dV - \int_{\partial\mathcal{B}_t} \boldsymbol{\eta} \cdot \mathbf{t} dA = 0 \tag{58}$$

for all $\boldsymbol{\eta} \in \mathcal{V}_u$.

Next, we consider the spaces of pore pressures as

$$\mathcal{C}_{p_i} = \{p_i : \mathcal{B} \rightarrow \mathbb{R} | p_i \in H^1, p_i = p_i^* \text{ on } \partial\mathcal{B}_{p_i}\}, \quad i = M, m \tag{59}$$

and the spaces of variations

$$\mathcal{V}_{\phi_i} = \{\phi_i : \mathcal{B} \rightarrow \mathbb{R} | \phi_i \in H^1, \phi_i = 0 \text{ on } \partial\mathcal{B}_{p_i}\}, \quad i = M, m. \tag{60}$$

The variational form of balance of fluid mass takes the form (no sum on i)

$$\int_{\mathcal{B}} \phi_i (\dot{\rho}_0^i + a_0) dV - \int_{\mathcal{B}} \text{GRAD } \phi^i \cdot \mathbf{Q}_i dV + \int_{\partial\mathcal{B}_{q_i}} \phi^i Q_i dA = 0 \tag{61}$$

for all $\phi_i \in \mathcal{V}_{\phi_i}$, where

$$a_0 = \begin{cases} c_0, & \text{if } i = M, \\ -c_0, & \text{if } i = m. \end{cases} \tag{62}$$

Alternatively, the variational equation for the balance of linear momentum can be written in terms of the symmetric Kirchhoff effective stress tensor as

$$\int_{\mathcal{B}} \nabla^s \boldsymbol{\eta} : \bar{\boldsymbol{\tau}} dV - \int_{\mathcal{B}} \nabla \cdot \boldsymbol{\eta} \bar{p} dV - \int_{\mathcal{B}} \rho_0 \boldsymbol{\eta} \cdot \mathbf{G} dV \tag{63}$$

$$+ \int_{\mathcal{B}} c_0(\tilde{\mathbf{v}}_m - \tilde{\mathbf{v}}_M) dV = \int_{\partial\mathcal{B}_t} \boldsymbol{\eta} \cdot \mathbf{t} dA \tag{64}$$

for all $\boldsymbol{\eta} \in \mathcal{V}_u$. As for the variational equation for fluid mass conservation, we can use the backward implicit scheme to write the variational equation in the time-integrated form

$$\int_{\mathcal{B}} \phi_i (\rho_0^i - \rho_{0n}^i) dV - \Delta t \rho_w \int_{\mathcal{B}} \nabla \phi^i \cdot J \tilde{\mathbf{v}}_i dV - \Delta t \int_{\mathcal{B}} \phi^i a_0 dV = -\Delta t \int_{\partial \mathcal{B}_{q_i}} \phi^i Q_i dA, \quad (65)$$

for all $\phi_i \in \mathcal{V}_{\phi_i}$, where $\Delta t = t - t_n$ is the step size.

3.3. Linearized variational equations

Before developing the linearized variation equations, we first introduce Darcy's law so as to reduce the finite element equations to $\mathbf{u}/p_M/p_m$ form. For double-porosity media, Darcy's law takes the form

$$J \tilde{\mathbf{v}}_M = -\mathbf{K}_M \cdot \nabla \mathcal{U}_M, \quad J \tilde{\mathbf{v}}_m = -\mathbf{K}_m \cdot \nabla \mathcal{U}_m, \quad (66)$$

where \mathcal{U}_M and \mathcal{U}_m are the fluid potentials in the macropores and micropores, respectively, given by

$$\mathcal{U}_M = \frac{p_M}{\rho_w g} + z, \quad \mathcal{U}_m = \frac{p_m}{\rho_w g} + z, \quad (67)$$

where z is the elevation axis and g is the gravity acceleration constant. Assuming isotropy in permeability, the pullback permeability tensor \mathbf{K} can be expressed in terms of effective grain diameter D and Jacobian J through an equation of the form

$$\mathbf{K}_M = K(D_M, J) \mathbf{1}, \quad \mathbf{K}_m = K(D_m, J) \mathbf{1} \quad (68)$$

where D_M is the effective diameter of the aggregates and D_m is the effective diameter of the grains in the micropores. An example of an empirical expression for the scalar function $K(D, J)$ is given by the well-known Kozeny–Carman equation [70]

$$K(D, J) = Jk(D, J), \quad k(D, J) = \frac{\rho_w g}{\mu_w} \frac{D^2}{180} \frac{(J - \phi_0^s)^3}{J(\phi_0^s)^2}, \quad (69)$$

where μ_w is the dynamic viscosity of water and ϕ_0^s is the volume fraction of the solid when $J = 1$. Alternatively, the Kozeny–Carman expression can be written in normalized form relative to the initial value of hydraulic conductivity and evolving according to J in a fashion similar to the equation above. In the examples discussed in this paper, the evolutions of hydraulic conductivities are expressed in terms of initial values k_{M0} and k_{m0} .

A second constitutive law leading to the $\mathbf{u}/p_M/p_m$ formulation determines the mass transfer term $c = c_0/J$ (see Eq. (51)) in terms of the fluid pressure jump. A vast number of studies have advanced constitutive relations for this term (see e.g., [71–76]). Here, we adopt the constitutive law used by Choo et al. [53] of the form

$$c = \frac{\bar{\alpha}}{\mu_w} (p_M - p_m), \quad (70)$$

where $\bar{\alpha}$ is a dimensionless parameter that depends on the characteristics of the interface between the macropores and micropores, such as permeability, spacing, and shape. This parameter can be determined either by an equation that takes permeability and pore geometry into account (e.g. [73]), or by inversion of test data (e.g. [77]).

We now consider a constitutive equation for the effective Kirchhoff stress of the form

$$\bar{\boldsymbol{\tau}} = \bar{\boldsymbol{\tau}}(\mathbf{u}, p_M, p_m). \quad (71)$$

Strictly speaking, $\bar{\boldsymbol{\tau}}$ is also a function of the pore fraction ψ , but this variable also depends on the independent variables \mathbf{u} , p_M , and p_m . Linearizing this stress tensor yields

$$\delta \bar{\boldsymbol{\tau}} = \boldsymbol{\alpha} : \nabla \delta \mathbf{u} + \mathbf{a}_M \delta p_M + \mathbf{a}_m \delta p_m, \quad (72)$$

where $\boldsymbol{\alpha}$ is a tangential moduli tensor discussed in the next section, and $\mathbf{a}_i = \partial \bar{\boldsymbol{\tau}} / \partial p_i$ for $i = M, m$. Furthermore, from Eq. (44) the pullback total mass density has the linearization

$$\delta \rho_0 = \delta \rho_0^M + \delta \rho_0^m = \rho_w \delta J, \quad (73)$$

where $\delta J = J \nabla \cdot \delta \mathbf{u}$. This results in the following linearized variational equation for balance of momentum

$$\int_B \nabla \boldsymbol{\eta} : \mathbf{a} : \nabla \delta \mathbf{u} \, dV + \int_B \boldsymbol{\eta} : (\mathbf{a}_M \delta p_M + \mathbf{a}_m \delta p_m) \, dV - \int_B (\delta(\nabla \cdot \boldsymbol{\eta}) \bar{p} + \nabla \cdot \boldsymbol{\eta} \delta \bar{p}) \, dV - \int_B \delta \rho_0 \boldsymbol{\eta} \cdot \mathbf{G} \, dV + \delta \int_B c \boldsymbol{\eta} \cdot (J \tilde{\mathbf{v}}_m - J \tilde{\mathbf{v}}_M) \, dV = \int_{\partial B} \boldsymbol{\eta} \cdot \delta \mathbf{t} \, dA, \tag{74}$$

where $\mathbf{a} = \boldsymbol{\alpha} - \bar{\boldsymbol{\tau}} \ominus \mathbf{1}$, $\delta(\nabla \cdot \boldsymbol{\eta}) = -\nabla \boldsymbol{\eta} : \delta \mathbf{u} \nabla$, and $c = c_0/J$, see the discussion surrounding Eq. (51). The stress term in the tangent moduli has components $(\bar{\boldsymbol{\tau}} \ominus \mathbf{1})_{ijkl} = \bar{\tau}_{il} \delta_{jk}$.

Eliminating the relative fluid velocities using Darcy’s law, and linearizing the associated volume integral, yields

$$\delta \int_B c \boldsymbol{\eta} \cdot (J \tilde{\mathbf{v}}_m - J \tilde{\mathbf{v}}_M) \, dV = \int_B c \boldsymbol{\eta} \cdot \delta(\mathbf{K}_M \cdot \nabla \mathcal{U}_M - \mathbf{K}_m \cdot \nabla \mathcal{U}_m) \, dV - \int_B \delta c \boldsymbol{\eta} \cdot (\mathbf{K}_M \cdot \nabla \mathcal{U}_M - \mathbf{K}_m \cdot \nabla \mathcal{U}_m) \, dV. \tag{75}$$

Disregarding the subscripts, we note that

$$\delta(\mathbf{K} \cdot \nabla \mathcal{U}) = \delta \mathbf{K} \cdot \nabla \mathcal{U} + \mathbf{K} \cdot \delta(\nabla \mathcal{U}), \tag{76}$$

where

$$\delta \mathbf{K} = (K'(J) \delta J) \mathbf{1}, \quad \delta(\nabla \mathcal{U}) = \nabla \delta p - \nabla p \cdot \nabla \delta \mathbf{u}. \tag{77}$$

Furthermore,

$$\delta c = \frac{\bar{\alpha}}{\mu_w} (\delta p_M - \delta p_m). \tag{78}$$

See Song and Borja [68] for further details on these derivatives.

Next we consider the linearization of the time-integrated variational equation for the balance of fluid mass. For pore scale $i = M, m$, we have

$$\int_B \phi_i \delta \rho_0^i \, dV - \Delta t \rho_w \delta \left(\int_B \nabla \phi^i \cdot \mathbf{K}_i \cdot \nabla \mathcal{U} \, dV \right) - \Delta t \int_B \phi^i \delta a_0 \, dV = -\Delta t \int_{\partial B_{q_i}} \phi^i \delta Q_i \, dA, \tag{79}$$

where δa_0 follows from (78) and $\delta \rho_0^i$ follows from (45) and (46). The flux term has the linearization

$$\delta \left(\int_B \nabla \phi^i \cdot \mathbf{K}_i \cdot \nabla \mathcal{U} \, dV \right) = \int_B \delta(\nabla \phi^i) \cdot \mathbf{K}_i \cdot \nabla \mathcal{U} \, dV + \int_B \nabla \phi^i \cdot \mathbf{K}_i \cdot \delta(\nabla \mathcal{U}) \, dV + \int_B \nabla \phi^i \cdot \delta \mathbf{K}_i \cdot \nabla \mathcal{U} \, dV, \tag{80}$$

where

$$\delta(\nabla \phi^i) = -\nabla \phi^i \cdot \nabla \delta \mathbf{u}. \tag{81}$$

It remains to determine the tangent operators $\boldsymbol{\alpha}$, \mathbf{a}_M and \mathbf{a}_m in Eq. (74); these are developed in the next section.

4. Discrete formulation

This section describes the discrete evolution of the pore fraction ψ , which measures the internal structure in a double-porosity material, as well as its impact on the effective stress tensor $\bar{\boldsymbol{\tau}}$. For constitutive modeling of the solid material, we employ the classic three-invariant hyperelasto-plasticity and solve the local unknowns in principal elastic strain space, see [55].

4.1. Stress-point integration

We recall the classic stress-point integration for finite deformation hyper-elastoplasticity consisting of an elastic predictor for the elastic left Cauchy–Green deformation tensor \mathbf{b}^e , followed by a plastic corrector in elastic logarithmic

principal strains [55]. The elastic predictor is calculated from the relative deformation gradient $\mathbf{f} = \partial \mathbf{x} / \partial \mathbf{x}_n$ and the current value of the elastic left Cauchy–Green deformation tensor \mathbf{b}_n^e , after which a spectral decomposition is performed, i.e.

$$\mathbf{b}^{e\text{tr}} = \mathbf{f} \cdot \mathbf{b}_n^e \cdot \mathbf{f}^T = \sum_{A=1}^3 (\lambda_A^{e\text{tr}})^2 \mathbf{m}^{(A)}, \tag{82}$$

where $\lambda_A^{e\text{tr}}$ is the trial elastic principal stretch with an associated principal direction $\mathbf{n}^{(A)}$ and spectral direction $\mathbf{m}^{(A)} = \mathbf{n}^{(A)} \otimes \mathbf{n}^{(A)}$. By coaxiality of $\mathbf{b}^{e\text{tr}}$ and $\bar{\boldsymbol{\tau}}$, we have

$$\bar{\boldsymbol{\tau}} = \sum_{A=1}^3 \bar{\tau}_A \mathbf{m}^{(A)}, \tag{83}$$

where $\bar{\tau}_A$ is a principal value of the effective Kirchhoff stress tensor obtained from the hyperelastic constitutive equation

$$\bar{\tau}_A = \frac{\partial \Psi^e}{\partial \varepsilon_A^e}, \quad \varepsilon_A^e = \log(\lambda_A^e), \tag{84}$$

in which Ψ^e is the stored energy function and ε_A^e is the elastic logarithmic principal strain determined from the logarithm of the elastic principal stretch λ_A^e . The stress-point integration algorithm entails the determination of the evolution of ε_A^e along with those of the internal state variables including the pore fraction ψ .

The local stress-point integration is as follows. Given the following starting values at t_n : $(\bar{\tau}_A)_n$ for $A = 1, 2, 3$; $(p_M)_n$, $(p_m)_n$, micropore fraction ψ_n , and preconsolidation pressures $(p_{cM})_n$ and $(p_{cn})_n$; and given increments $\Delta \mathbf{u}$, Δp_M , and Δp_m ; find the principal stresses $\bar{\tau}_A \equiv (\bar{\tau}_A)_{n+1}$ for $A = 1, 2, 3$, and micropore fraction $\psi \equiv \psi_{n+1}$. To accommodate nonlinear hyperelasticity we use the notion of residuals and perform a return mapping in principal logarithmic elastic strain space as follows:

$$r_A = \varepsilon_A^e - \varepsilon_A^{e\text{tr}} + \Delta \lambda \frac{\partial F}{\partial \bar{\tau}_A} \rightarrow 0, \quad A = 1, 2, 3, \tag{85}$$

where $\varepsilon_A^{e\text{tr}} = \log(\lambda_A^{e\text{tr}})$ and $\Delta \lambda$ is the incremental plastic consistency parameter. Next, we impose the yield criterion

$$r_4 = F(\bar{\tau}_1, \bar{\tau}_2, \bar{\tau}_3, \bar{p}_c) \rightarrow 0, \tag{86}$$

where \bar{p}_c is the mean preconsolidation pressure defined from the hardening law

$$r_5 = \bar{p}_c - \psi p_{cm} \left(\psi, \sum_{A=1}^3 \varepsilon_A^e \right) - (1 - \psi) p_{cM} \left(\psi, \sum_{A=1}^3 \varepsilon_A^{e\text{tr}} \right) \rightarrow 0. \tag{87}$$

The final residual term is the thermodynamic restriction

$$r_6 = p_{cm} \left(\psi, \sum_{A=1}^3 \varepsilon_A^e, \sum_{A=1}^3 \varepsilon_A^{e\text{tr}} \right) - p_{cM} \left(\psi, \sum_{A=1}^3 \varepsilon_A^{e\text{tr}} \right) + (p_M - p_m) \rightarrow 0, \tag{88}$$

where $p_M = (p_M)_n + \Delta p_M$ and $p_m = (p_m)_n + \Delta p_m$. It must be noted that in the above equations, the evolutions of $\varepsilon_A^{e\text{tr}}$ (for $A = 1, 2, 3$), p_M , and p_m are all given, and thus, we have a total of six residual equations in six unknowns, namely, ε_A^e ($A = 1, 2, 3$), $\Delta \lambda$, \bar{p}_c , and ψ .

The six unknowns are solved by a local Newton iteration. Setting

$$\mathbf{r} = \begin{Bmatrix} r_1 \\ r_2 \\ r_3 \\ r_4 \\ r_5 \\ r_6 \end{Bmatrix}, \quad \mathbf{x} = \begin{Bmatrix} \varepsilon_1^e \\ \varepsilon_2^e \\ \varepsilon_3^e \\ \Delta \lambda \\ \bar{p}_c \\ \psi \end{Bmatrix}, \quad \mathbf{A} = \mathbf{r}'(\mathbf{x}), \tag{89}$$

the problem is then to find the solution \mathbf{x}^* such that $\mathbf{r} = \mathbf{0}$. The elements of the local tangent operator $\mathbf{r}'(\mathbf{x})$ are developed in [Appendix A](#).

4.2. Tangent operators

In this section we develop expressions for the global tangent operators accommodating the variation of the pore fraction ψ . The key aspect to obtaining these tangent operators is the consistent linearization of the local residual vector \mathbf{r} in (89) through the local tangent operator \mathbf{A} , which is available in closed form as shown in the [Appendix A](#).

Consider the functional representation of $\bar{\boldsymbol{\tau}}$ in terms of \mathbf{u} , p_M , and p_m as indicated in (71), and its spectral representation shown in (83). We note that the spectral directions of $\bar{\boldsymbol{\tau}}$ depend on \mathbf{u} alone through $\mathbf{b}^{e\text{tr}}$, whereas its principal values depend not only on ε_A^e but also on p_M and p_m , all of them through the principal elastic logarithmic strains ε_A^e for $A = 1, 2, 3$. Therefore, we can write the variation of $\bar{\boldsymbol{\tau}}$ as

$$\delta \bar{\boldsymbol{\tau}} = \sum_{A=1}^3 \left(\delta \bar{\tau}_A \mathbf{m}^{(A)} + \bar{\tau}_A \delta \mathbf{m}^{(A)} \right), \tag{90}$$

where

$$\begin{aligned} \delta \bar{\tau}_A &= \sum_{C=1}^3 \frac{\partial \bar{\tau}_A}{\partial \varepsilon_C^e} \left(\sum_{B=1}^3 \frac{\partial \varepsilon_C^e}{\partial \varepsilon_B^{e\text{tr}}} \delta \varepsilon_B^{e\text{tr}} + \frac{\partial \varepsilon_C^e}{\partial p_M} \delta p_M + \frac{\partial \varepsilon_C^e}{\partial p_m} \delta p_m \right) \\ &= \sum_{B=1}^3 a_{AB} \delta \varepsilon_B^{e\text{tr}} + \frac{\partial \bar{\tau}_A}{\partial p_M} \delta p_M + \frac{\partial \bar{\tau}_A}{\partial p_m} \delta p_m, \end{aligned} \tag{91}$$

and

$$\begin{aligned} a_{AB} &= \sum_{C=1}^3 a_{AC}^e \frac{\partial \varepsilon_C^e}{\partial \varepsilon_B^{e\text{tr}}}, & \frac{\partial \bar{\tau}_A}{\partial p_M} &= \sum_{C=1}^3 a_{AC}^e \frac{\partial \varepsilon_C^e}{\partial p_M}, \\ \frac{\partial \bar{\tau}_A}{\partial p_m} &= \sum_{C=1}^3 a_{AC}^e \frac{\partial \varepsilon_C^e}{\partial p_m}, & a_{AC}^e &= \frac{\partial \bar{\tau}_A}{\partial \varepsilon_C^e} = \frac{\partial^2 \Psi^e}{\partial \varepsilon_A^e \partial \varepsilon_C^e}. \end{aligned} \tag{92}$$

Furthermore, the spin of $\bar{\boldsymbol{\tau}}$ is the same as the spin of $\mathbf{b}^{e\text{tr}}$, and so,

$$\sum_{A=1}^3 \bar{\tau}_A \delta \mathbf{m}^{(A)} = \sum_{A=1}^3 \sum_{B \neq A} \omega_{AB} (\bar{\tau}_B - \bar{\tau}_A) \mathbf{m}^{(AB)}, \tag{93}$$

where ω_{AB} is the spin of $\mathbf{b}^{e\text{tr}}$, and $\mathbf{m}^{(AB)} = \mathbf{n}^{(A)} \otimes \mathbf{n}^{(B)}$.

The relevant tangent operators of interest, defined in (72), then take the following forms

$$\begin{aligned} \boldsymbol{\alpha} &= \sum_{A=1}^3 \sum_{B=1}^3 a_{AB} \mathbf{m}^{(A)} \otimes \mathbf{m}^{(B)} + \sum_{A=1}^3 \sum_{B \neq A} \frac{\bar{\tau}_B - \bar{\tau}_A}{(\lambda_B^{e\text{tr}})^2 - (\lambda_A^{e\text{tr}})^2} \boldsymbol{\beta}_{AB}, \\ \boldsymbol{\beta}_{AB} &= (\lambda_B^{e\text{tr}})^2 \mathbf{m}^{(AB)} \otimes \mathbf{m}^{(AB)} + (\lambda_A^{e\text{tr}})^2 \mathbf{m}^{(AB)} \otimes \mathbf{m}^{(BA)}, \\ \mathbf{a}_M &= \sum_{A=1}^3 \frac{\partial \bar{\tau}_A}{\partial p_M} \mathbf{m}^{(A)}, & \mathbf{a}_m &= \sum_{A=1}^3 \frac{\partial \bar{\tau}_A}{\partial p_m} \mathbf{m}^{(A)}. \end{aligned} \tag{94}$$

Complete development of the tangent operators relies on closed-form expressions for the derivatives of ε_A^e .

Consider the converged residual equation of the local problem, $\mathbf{r}(\mathbf{x}^*) = \mathbf{0}$. We recall that this residual equation relies on the assumption that $\varepsilon_A^{e\text{tr}}$, p_M , and p_m are all given. Thus, the residual vector may be viewed as a function of

\mathbf{z} as well, i.e., $\mathbf{r} = \mathbf{r}(\mathbf{z}, \mathbf{x})$, where

$$\mathbf{z} := \begin{Bmatrix} \varepsilon_1^{\text{e tr}} \\ \varepsilon_2^{\text{e tr}} \\ \varepsilon_3^{\text{e tr}} \\ p_M \\ p_m \end{Bmatrix} \quad \text{and} \quad \left. \frac{\partial \mathbf{r}}{\partial \mathbf{z}} \right|_{\mathbf{x}^*} + \mathbf{A} \left. \frac{\partial \mathbf{x}}{\partial \mathbf{z}} \right|_{\mathbf{x}^*} = \mathbf{0}. \quad (95)$$

In the foregoing equation, it is understood that $\mathbf{r}(\mathbf{z}, \mathbf{x}^*) = \mathbf{0}$, and thus, all the derivatives must be evaluated at $\mathbf{x} = \mathbf{x}^*$. This equation then yields the tangent matrix

$$\mathbf{B} := \frac{\partial \mathbf{x}}{\partial \mathbf{z}} = -\mathbf{A}^{-1} \left. \frac{\partial \mathbf{r}}{\partial \mathbf{z}} \right|_{\mathbf{x}}. \quad (96)$$

The derivatives of interest can be obtained from the elements of the matrix \mathbf{B} ,

$$\frac{\partial \varepsilon_I^{\text{e}}}{\partial \varepsilon_J^{\text{e tr}}} = B_{IJ}, \quad \frac{\partial \varepsilon_I^{\text{e}}}{\partial p_M} = B_{I4}, \quad \frac{\partial \varepsilon_I^{\text{e}}}{\partial p_m} = B_{I5}, \quad (97)$$

for $I, J = 1, 2, 3$. Elements in the upper 3×5 block of the matrix \mathbf{B} define all the required derivatives of ε_I^{e} . The components of the tangent matrix $\partial \mathbf{r} / \partial \mathbf{z}$ are derived in [Appendix B](#).

4.3. Yield function

We use a three-invariant plasticity model derived from enhancing the two-invariant modified Cam-Clay theory. The three invariants of the effective Kirchhoff stress tensor $\bar{\boldsymbol{\tau}}$ are

$$\tau_m = \frac{1}{3} \text{tr}(\bar{\boldsymbol{\tau}}) \leq 0, \quad q = \sqrt{\frac{3}{2}} \|\boldsymbol{\xi}\|, \quad \frac{1}{\sqrt{6}} \cos 3\theta = \frac{\text{tr}(\boldsymbol{\xi}^3)}{\text{tr}(\boldsymbol{\xi}^2)^{3/2}}, \quad (98)$$

where $\boldsymbol{\xi} = \bar{\boldsymbol{\tau}} - \tau_m \mathbf{1}$. The yield function is of the form (see [\[55\]](#))

$$F = \zeta^2 \frac{q^2}{M^2} + \tau_m (\tau_m - \bar{p}_c) \leq 0, \quad (99)$$

where $M > 0$ is the slope of the critical stress line, and ζ is the scaling function of the form [\[78,79\]](#)

$$\zeta(\rho, \theta) = \frac{(1 + \rho) + (1 - \rho) \cos 3\theta}{2\rho}. \quad (100)$$

The parameter ρ should be in the range $7/9 \leq \rho \leq 1$ to guarantee smoothness and convexity. An associative flow rule is assumed throughout.

5. Numerical examples

The objectives of this section are twofold: (a) to show that the proposed double-porosity formulation can predict the experimental observations well, and (b) to demonstrate the robust aspects of the algorithm in handling the concurrent transient fluid pressure dissipation and an evolving internal structure.

5.1. Stress-point simulations

As a first example, we conduct stress-point simulations of the compression of two aggregated soils, namely, Bioley silt and Corinth marl. The goal of the experiments was to investigate the compressibility characteristics of these two aggregated soils under ‘drained’ condition where $\bar{p}_c = p_{cM} = p_{cm}$. Because there is no transient pore pressure dissipation to consider, it suffices to treat the soil sample as a homogeneously deforming element and conduct stress-point simulations on this element.

Koliji et al. [\[31\]](#) investigated the compressibility characteristics of an aggregated Bioley silt under a 1D compression test in which the lateral strain was held fixed while the sample was compressed vertically. The experiment entailed

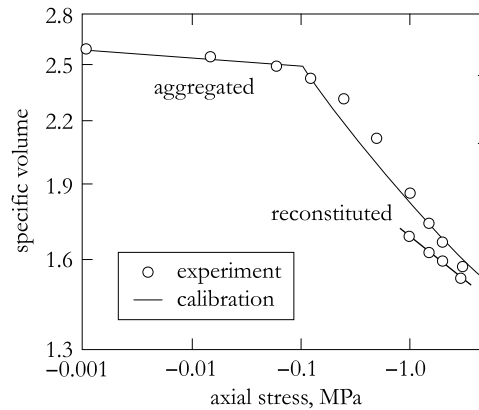


Fig. 3. Variation of specific volume with axial stress for aggregated and reconstituted Bioley silt. Experimental data from Koliji et al. [31].

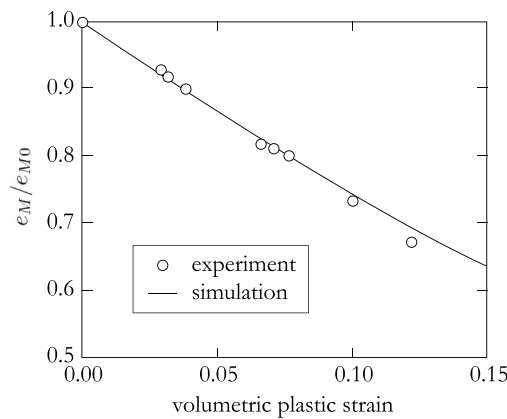


Fig. 4. Variation of macropore void ratio e_M with volumetric plastic strain for Bioley silt. Initial value e_{M0} was calculated at a stress level equal to $\bar{p}_c = -100$ kPa. Experimental data from Koliji et al. [31].

measuring the compressibility indices c_c and c_r for the reconstituted soil, as well as the compressibility index c_M for the aggregated (structured) soil. Fig. 3 shows the relevant experimental data for the structured soil with a preconsolidation pressure of $\bar{p}_c = -100$ kPa, as well as for the reconstituted soil [31]. From these data, the following compressibility indices were determined: $c_c = 0.085$, $c_r = 0.009$, and $c_M = 0.4$. Note that the macropores do not exhibit elastic deformations, and so all recoverable deformations can be attributed solely to the micropore deformations.

Koliji et al. [29] then used neutron tomography to investigate the evolution of the macropore void ratio e_M as a function of the overall plastic volumetric strain for the same Bioley silt sample. Fig. 4 shows the experimental data along with the evolution of e_M predicted by the proposed constitutive formulation. Very good agreement can be observed.

Next we consider a similar 1D compression test conducted by Anagnostopoulos et al. [51] on an aggregated sample of Corinth marl. Their testing program also included triaxial testing on the same soil in addition to 1D compression testing. Predicting the triaxial responses of this soil using parameters calibrated from the 1D compression test is a challenge since the two stress conditions are vastly different. The following discussions compare the triaxial responses predicted by the proposed constitutive framework with those reported previously in the literature.

Fig. 5 shows the experimental data from 1D compression tests on aggregated and reconstituted samples of Corinth marl [51]. From these data, the following compressibility indices have been determined for this soil: $c_c = 0.046$, $c_r = 0.004$, and $c_M = 0.8$. Using these parameters, the triaxial test was then simulated as a stress-point problem and the results are shown in Figs. 6–9. We observe that the proposed constitutive formulation predicted both the deviator stress–axial strain and volumetric strain–axial strain responses reasonably well. In contrast, the model proposed by

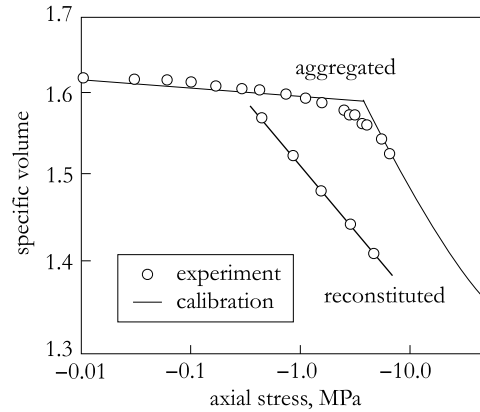


Fig. 5. Variation of specific volume with axial stress for aggregated and reconstituted Corinth marl. Experimental data from Anagnostopoulos et al. [51].

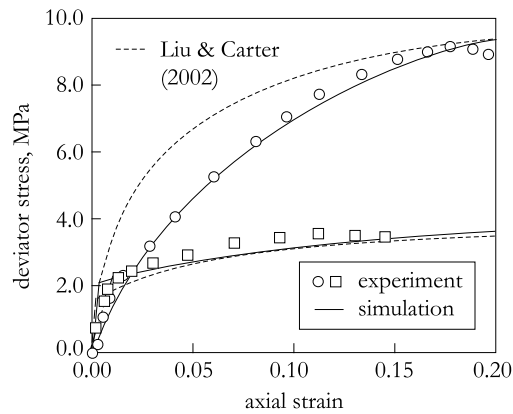


Fig. 6. Deviator stress versus axial strain for Corinth marl: comparison with Liu and Carter [27]. Experimental data from Anagnostopoulos et al. [51]: open circles are for test at confining pressure of 4 MPa, open squares at 1.5 MPa.

Liu and Carter [27] significantly overpredicted the deviator stress at a confining pressure of 4 MPa (Fig. 6), and also overpredicted the volumetric strain at a confining pressure of 1.5 MPa (Fig. 7). On the other hand, the constitutive framework proposed by Koliji et al. [25] captured the deviator stress–axial strain responses just as accurately as the proposed constitutive model (Fig. 8); however, their model underpredicted the volumetric compression at both confining pressures considerably (Fig. 9). For the two soils considered, the proposed constitutive formulation appears to adapt to other stress conditions more accurately.

5.2. 1D consolidation with secondary compression

Several investigators have argued that secondary compression in clays can be attributed in part to delayed dissipation of excess pore pressures in the micropores of multiple porosity media [80–82]. Considering that many aggregated soils such as peat show pronounced secondary consolidation, it is interesting to see if the proposed double-porosity formulation could indeed replicate such phenomena.

Fig. 10 shows the finite element mesh considered in the simulation of one-dimensional consolidation process in a soil with double porosity. The domain is 0.1 m wide and 1.0 m tall, and discretized into 20 quadrilateral mixed elements with biquadratic displacement interpolation of displacement and bilinear interpolation of the macropore and micropore pressures. The material parameters for the solid were assumed to be the same as those of Bioley silt presented in the previous example. The initial hydraulic conductivities for the macropores and micropores were taken as follows: $k_{M0} = 10^{-5}$ m/s and $k_{m0} = 10^{-9}$ m/s. The mass transfer term $\bar{\alpha}$ was assumed to be a linear function

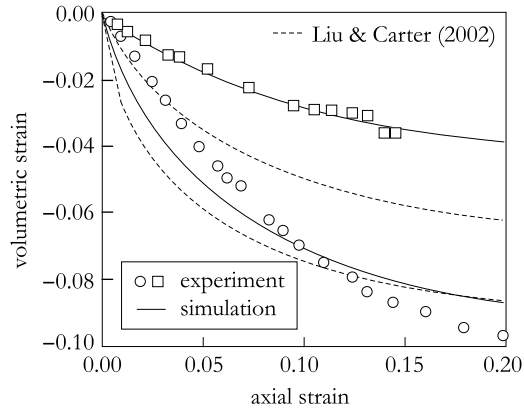


Fig. 7. Volumetric strain versus axial strain for Corinth marl: comparison with Liu and Carter [27]. Experimental data after Anagnostopoulos et al. [51], with open circles for test at confining pressure of 4 MPa, and open squares at 1.5 MPa.

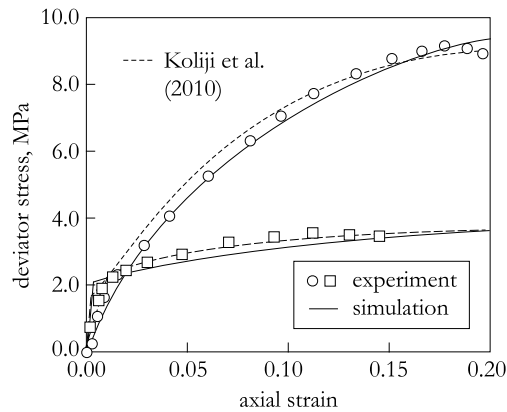


Fig. 8. Deviator stress versus axial strain responses for Corinth marl: comparison with Koliji et al. [25]. Experimental data from Anagnostopoulos et al. [51]: open circles are for test at confining pressure of 4 MPa, open squares at 1.5 MPa.

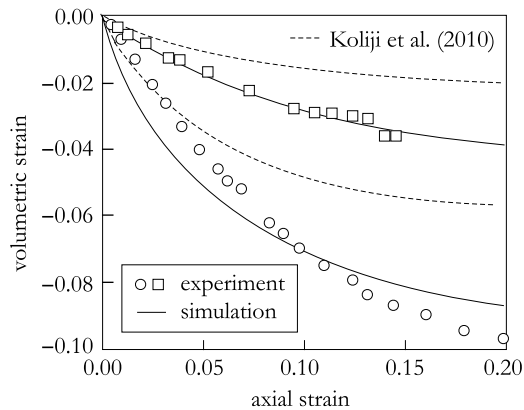


Fig. 9. Volumetric strain versus axial strain for Corinth marl: comparison with Koliji et al. [25]. Experimental data after Anagnostopoulos et al. [51], with open circles for test at confining pressure of 4 MPa, and open squares at 1.5 MPa.

of the micropore hydraulic conductivity, with two values considered to investigate its impact on the hydromechanical response: (a) $\bar{\alpha}/k_m = 10^2$ s/m, and (b) $\bar{\alpha}/k_m = 10^3$ s/m.

The initial condition was established, first, by subjecting the material to an isotropic compressive stress of 5 kPa, after which it was loaded to a vertical compressive stress of 200 kPa under fully drained condition on both the

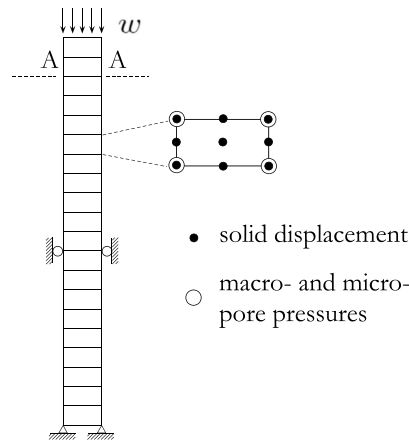


Fig. 10. Finite element mesh for 1D consolidation with secondary compression.

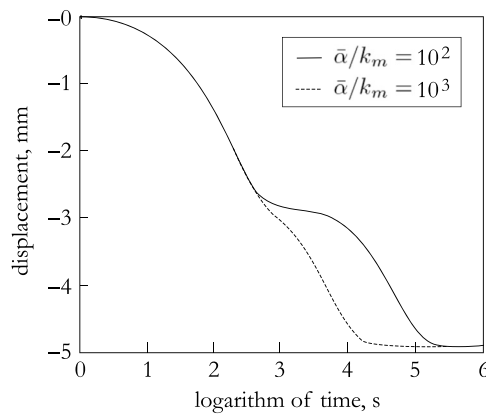


Fig. 11. Time evolution of vertical displacement at 0.1 m below the top boundary (level A–A) showing separation of scales. Values of $\bar{\alpha}/k_m$ in s/m.

macropores and micropores. Then, an additional downward load of $w = 10$ kPa was applied on top of the mesh while allowing fluid in the macropores to drain to the top surface and fluid in the micropores to drain into the macropores. In other words, the top surface was assumed to be a zero-pressure boundary for the macropores and a no-flow boundary for the micropores, which means that the micropores could only drain into the macropores but not through the top drainage boundary. The consolidation phase began with a time increment of 1 s and with subsequent increments magnified by a factor of 1.01, i.e., $\Delta t_{n+1} = 1.01\Delta t_n$.

Fig. 11 shows the time evolution of the vertical displacement at a point located 0.1 m from the top boundary (level A–A in Fig. 10). The shape of the curves suggests two stages of consolidation: a primary consolidation in which the macropores drain through the top boundary, followed by a secondary compression in which the micropores drain into the macropores. Note that for a sufficiently large mass transfer coefficient ($\bar{\alpha}/k_m = 10^3$ s/m) the secondary compression is not so pronounced; however, for a sufficiently small mass transfer coefficient ($\bar{\alpha}/k_m = 10^2$ s/m) the two stages of consolidation become very distinct. In the latter case, the first stage of consolidation had enough time to finish even before the second stage of compression could begin, producing a clear separation of scales in time domain.

For the same point at level A–A, Fig. 12 depicts the time evolution of the preconsolidation stresses \bar{p}_c , p_{cM} , and p_{cm} , relative to the initial value of \bar{p}_c . The macropore preconsolidation stress p_{cM} shows early hardening as the transient macropore water pressure p_M dissipates during the first stage of consolidation. However, the hardening response on p_{cM} is followed by mild softening as the transient micropore water pressure p_m dissipates and the micropore preconsolidation stress p_{cm} undergoes hardening during the second stage of consolidation. Between

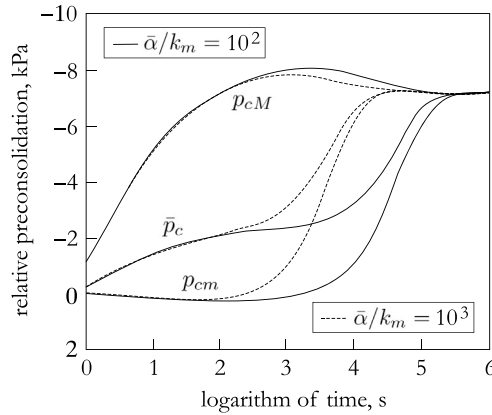


Fig. 12. Time evolution of preconsolidation stress, relative to the value of \bar{p}_c at time $t = 0$, at 0.1 m below the top boundary (level A–A). Values of $\bar{\alpha}/k_m$ in s/m.

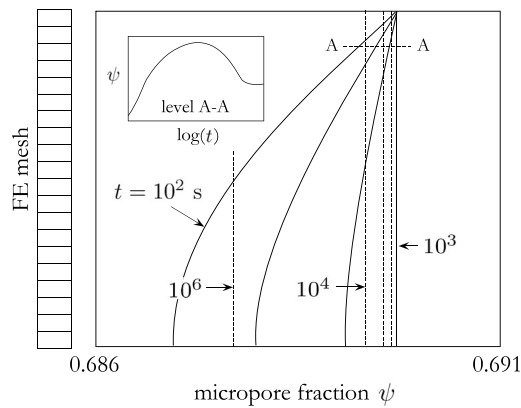


Fig. 13. Spatial and temporal evolution of ψ alongside the finite element mesh. Level A–A is 0.1 m below the top. Solid curves denote primary consolidation; dashed lines denote secondary compression.

$t = 10^5$ s and $t = 10^6$ s, all three preconsolidation stresses approach a common value as the transient pore water pressures in both the macropores and micropores dissipate. Results of this example indeed show that the proposed double-porosity formulation can capture the secondary compression attributed to the fluid dissipation in the micropores.

Fig. 13 portrays the spatial and temporal evolution of the internal structure variable ψ for $\bar{\alpha}/k_m = 10^2$ s/m. Between $t = 10^2$ s and $t = 10^3$ s, the spatial distribution resembles what one would expect from a typical one-dimensional consolidation curve, i.e., as the macropores compact, the micropore fraction ψ increases. At $t = 10^3$ s, the primary consolidation is essentially complete, and ψ is nearly uniform with depth. Beyond $t = 10^3$ s, secondary compression begins, producing nearly uniform compaction of the micropores with depth and a decrease in the value of ψ . Secondary compression appears to end at approximately $t = 10^6$ s. Once again, separation of scales is noted, in which the primary consolidation and secondary compression take place sequentially, due to the relatively small value of the mass transfer coefficient $\bar{\alpha}$ used in the simulation.

5.3. Secondary compression beneath a leaning tower

The third and final example illustrates the effect of secondary compression on the time-dependent tilting of a seven-storey tower. The finite element mesh for this example accommodates a condition of plane strain and is shown in Fig. 14. The foundation of the tower consists of a 10 m-thick sand layer underlain by a 30 m-thick clay layer. Under

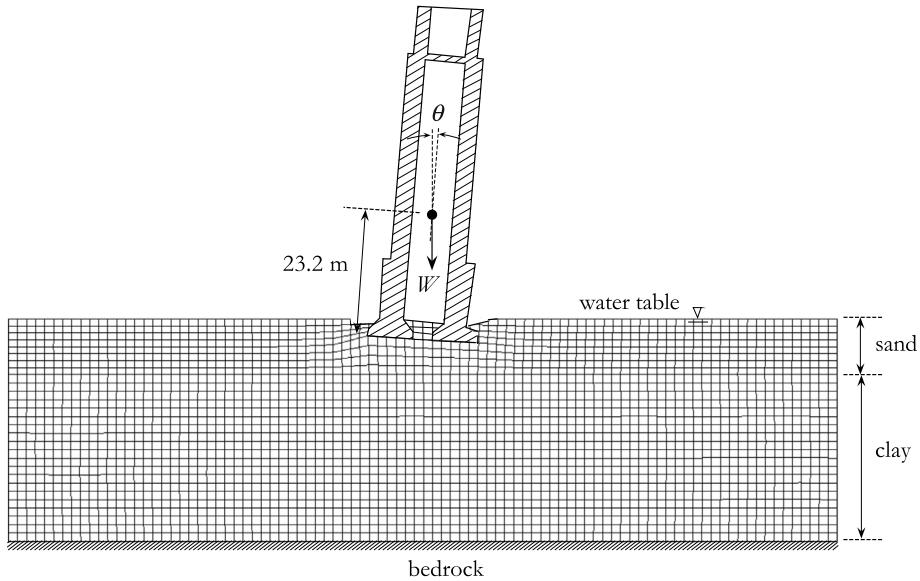


Fig. 14. Finite element mesh for foundation of a leaning tower: clay layer is modeled as a double-porosity material with dual permeability.

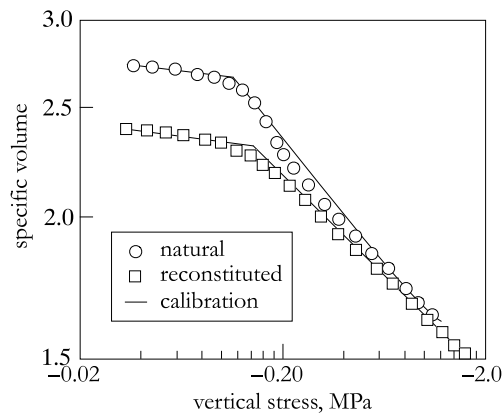


Fig. 15. Compressibility curves for natural and reconstituted Pancone clay. Experimental data from Callisto and Calabresi [83].

the clay layer is a rigid, impermeable bedrock. The ground water table is located at the top of the sand layer. The tower is assumed to be rigid with a distributed weight of $W = 6.6 \text{ MN/m}$ at 23.2 m from the base. We should note that this example is only a hypothetical problem, and that the finite element mesh shown in Fig. 14 should not be interpreted as a model for any actual tower.

The sand layer is assumed to be a Neo-Hookean material with a bulk modulus of 12 MPa, Poisson's ratio of 0.3, an effective (buoyant) unit weight of 1.0 Mg/m^3 , and a very high permeability. Hence, this layer may be assumed to be incapable of generating excess pore water pressure. The clay layer, on the other hand, is assumed to be a double-porosity material with similar properties to Pancone clay in Pisa, Italy, see [83]. Fig. 15 shows the natural compressibility of this clay, as well as the compressibility of the reconstituted material. The fact that the two compressibility curves are not one on top of the other implies that this particular clay exhibits double porosity to a certain extent. Based on these compressibility curves, we have calibrated the material parameters for the clay as $c_c = 0.176$, $c_r = 0.022$, $c_M = 0.6$, $\phi^M = 0.12$, and $\phi^m = 0.52$. The intrinsic mass densities for the solid and water are assumed to be 2.65 Mg/m^3 and 1.0 Mg/m^3 , respectively. The initial hydraulic conductivities of the macropores and micropores are assigned as $k_{M0} = 10^{-8} \text{ m/s}$ and $k_{m0} = 10^{-11} \text{ m/s}$, respectively, whereas the mass transfer coefficient has the value $\bar{\alpha}/k_m = 100 \text{ s/m}$.

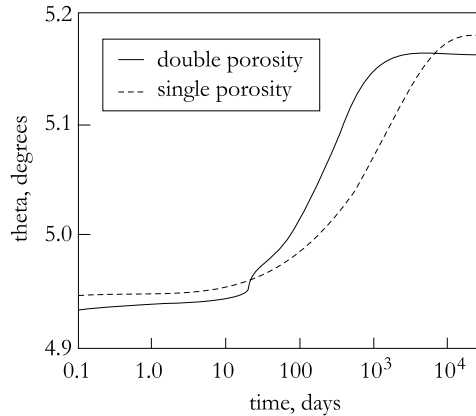


Fig. 16. Variation of tower inclination θ with time.

To begin the simulation, gravity load was first imposed on the foundation soil under ‘drained’ condition, i.e., with no excess pore fluid pressure developing. Since the Cam–Clay model does not allow a stress-free state, a very small initial isotropic compressive stress of 10 kPa (effective) was first specified at all Gauss integrations points. Once the soil was in static equilibrium under gravity, the overconsolidation ratio of the clay was set to 1.6 (i.e., the size of the yield surface at yield was multiplied by a factor of 1.6) to define a preloaded state. Then, the tower load W was applied under ‘undrained’ condition (i.e., no fluid flow). The tower was given a small geometrical tilt in the beginning so that by the time all of its weight was applied its inclination was around $\theta \approx 4.9^\circ$ from the vertical, see Fig. 14. Under this sustained tower weight, the fluid pressure in the soil was allowed to dissipate, causing the tower to tilt further with time.

Fig. 16 shows the time-evolution of the angle θ after all of the tower weight has been applied. For comparison, we also present the result obtained with single-porosity formulation in which the clay was assumed to have a hydraulic conductivity equal to the volume-average of the hydraulic conductivities of the macropores and micropores. Observe that the double-porosity simulation predicts faster rate of fluid pressure dissipation, with the tower reaching a steady-state tilt at $t \approx 10^3$ days. This is to be expected since the higher permeability in the macropores would make drainage easier for the same drainage path, whereas the micropores would have a shorter effective drainage path since they could drain directly into the macropores. Also note that separation of scales in time is evident even on the inclination-time response, with the onset of secondary compression in the form of rapid change in slope noted at time $t \approx 20$ days. The double-porosity simulation also predicted slightly different tower tilt at steady state, resulting primarily from the fact that porosity changes in the macropores and micropores were tracked separately whereas the single-porosity simulation did not account for these changes explicitly.

Figs. 17 and 18 show the time-evolution of the macropore and micropore fluid pressures, p_M and p_m , respectively. Observe that p_M appears to decrease monotonically with time everywhere (Fig. 17), whereas p_m exhibits the so-called Mandel–Cryer effect in the vicinity of the tower base. This effect is characterized by a momentary increase in the fluid pressure (note the more intense red region at $t \approx 1$ day) before it subsequently dissipates (Fig. 18). On the other hand, Fig. 19 depicts the time-evolution of the internal structure variable ψ . The figure suggests a significant increase of the micropore fraction in the vicinity of the tower base at time $t \approx 40$ days due to compression of the macropores, followed by a subsequent decrease at time $t \approx 400$ days due to compression of the micropores. In general, this sequential compression of the macropores and micropores is similar to the phenomenon of primary/secondary compression observed in the 1D consolidation example of the previous section.

6. Closure

We have presented a novel constitutive framework for solid deformation and fluid flow in a porous material exhibiting two porosity scales. A unique feature of the framework is the separate treatment of hardening in the macropores and micropores arising from fluid flow through these two pore scales. This allows the evolution of the internal structure, herein represented by the micropore fraction ψ , to be defined concurrently with fluid flow and solid deformation. The formulation has been validated against experimental data on aggregated soils, and has been

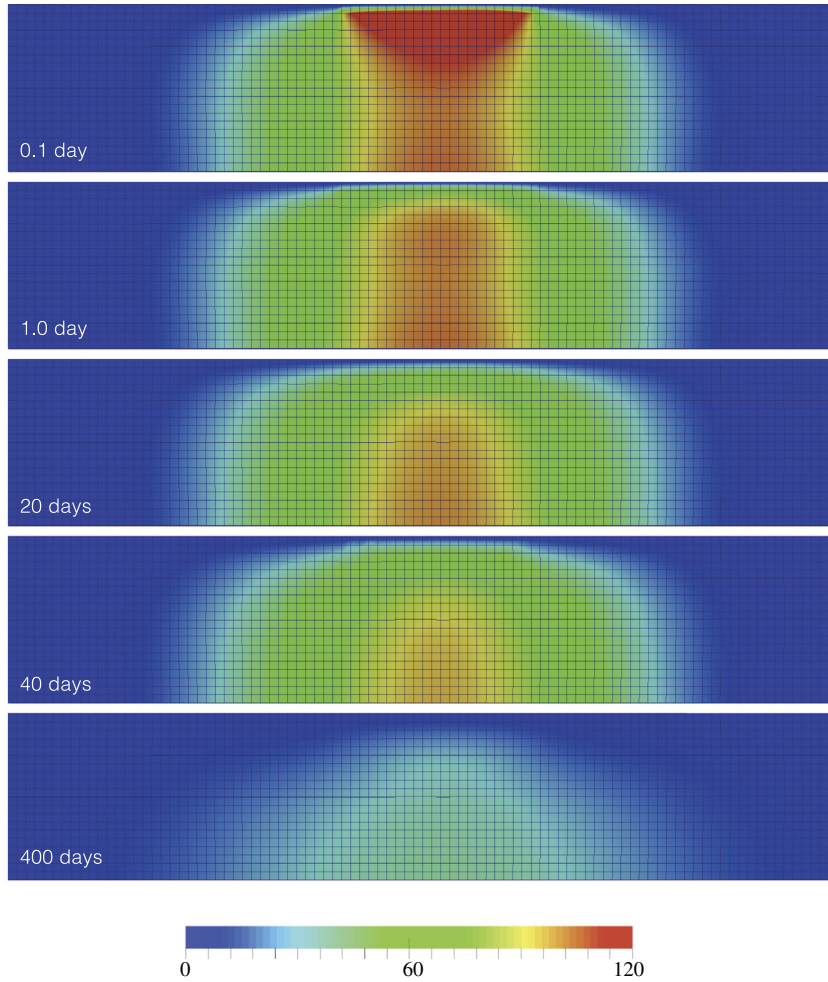


Fig. 17. Evolution of macropore pressure p_M within the clay layer. Color bar in kPa. (For interpretation of the references to color in this figure legend, the reader is referred to the web version of this article.)

implemented into a finite element code utilizing a $\mathbf{u}/p_M/p_m$ formulation. Many aggregated soils such as peat and highly compressible clays show pronounced secondary consolidation. This paper demonstrates that such phenomenon may be interpreted in the context of double-porosity problem as secondary compression attributed in part to delayed dissipation of excess pore pressures in the micropores, which is captured well by the proposed framework.

Acknowledgments

This material is based upon work supported by the U.S. Department of Energy, Office of Science, Office of Basic Energy Sciences, Geosciences Research Program, under Award Number DE-FG02-03ER15454. Analyses of laboratory soils data were conducted as part of a project sponsored by the National Science Foundation under Award Number CMMI-1462231. The second author acknowledges financial supports provided by the Fulbright Program, the John A. Blume Earthquake Engineering Center, and the Charles H. Leavell Graduate Student Fellowship.

Appendix A. Local tangent operator

We first note the tangential elastic constitutive equation

$$\delta \bar{\tau}_A = \sum_{B=1}^3 a_{AB}^e \delta \varepsilon_B^e, \quad (101)$$

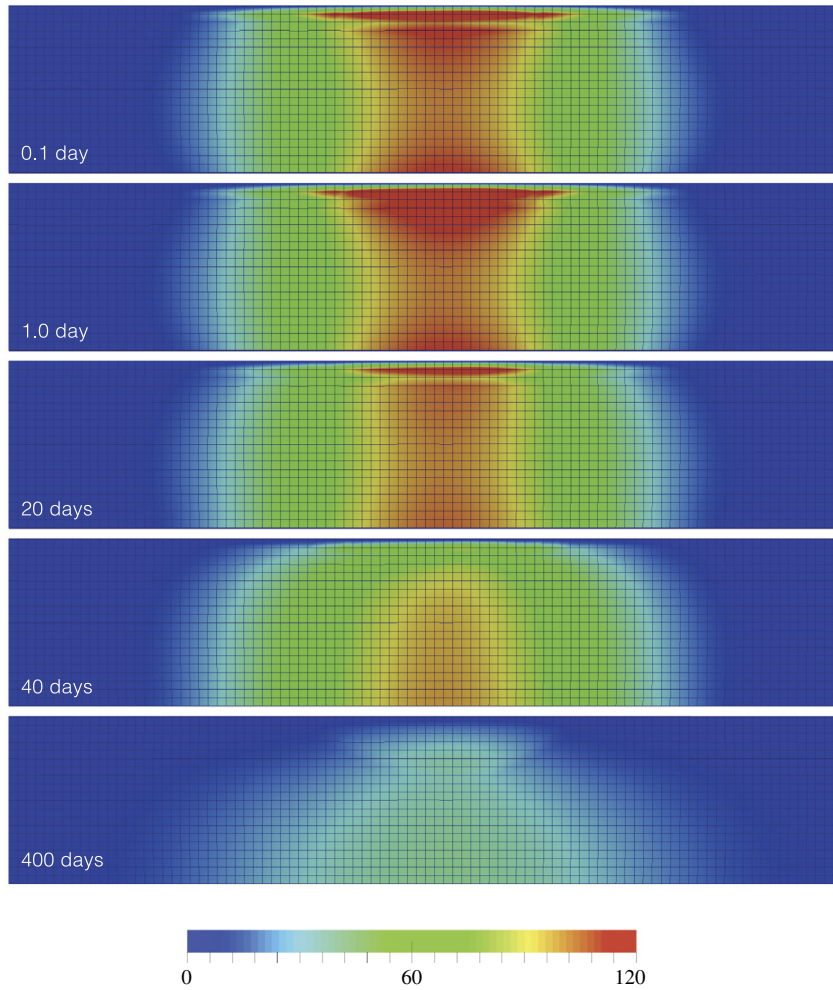


Fig. 18. Evolution of micropore pressure p_m within the clay layer. Color bar in kPa. (For interpretation of the references to color in this figure legend, the reader is referred to the web version of this article.)

where $a_{AB}^e = \partial^2 \Psi^e / \partial \varepsilon_A^e \partial \varepsilon_B^e$ is the tangential elasticity matrix in principal axes. Consider the local residual expression $\mathbf{r} = \mathbf{r}(\mathbf{x})$, where the components of \mathbf{r} are given in (85)–(88) and those of \mathbf{x} are given in (89). We note that for the local problem the values of $\varepsilon_A^{e\text{tr}}$, p_M , and p_m are given.

The local tangent operator $\mathbf{A} = \mathbf{r}'(\mathbf{x})$ has components given below. First, we consider the following derivatives with respect to $x_A = \varepsilon_A^e$ for $A = 1, 2, 3$:

$$A_{AB} = \delta_{AB} + \Delta\lambda \sum_{C=1}^3 \frac{\partial^2 F}{\partial \bar{\tau}_A \partial \bar{\tau}_C} a_{CB}^e, \quad B = 1, 2, 3. \tag{102}$$

The remaining derivatives for $A = 1, 2, 3$ are

$$A_{4A} = \sum_{B=1}^3 \frac{\partial F}{\partial \bar{\tau}_B} a_{BA}^e, \quad A_{5A} = -\psi \frac{\partial p_{cm}}{\partial \varepsilon_A^e}, \quad A_{6A} = \frac{\partial p_{cm}}{\partial \varepsilon_A^e}, \tag{103}$$

where $\partial p_{cm} / \partial \varepsilon_A^e = \partial p_{cm} / \partial \varepsilon_v^e$.

Next we consider derivatives with respect to $x_4 = \Delta\lambda$. For $A = 1, 2, 3$, we have

$$A_{A4} = \frac{\partial F}{\partial \bar{\tau}_A}, \quad A_{44} = A_{54} = A_{64} = 0. \tag{104}$$

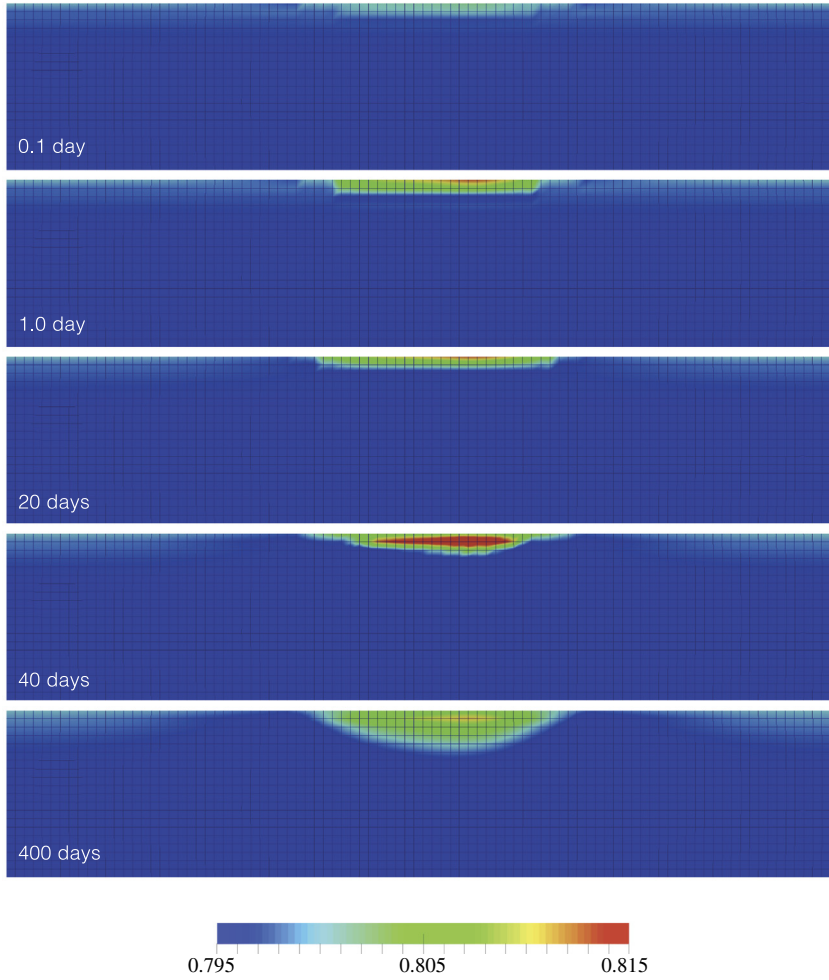


Fig. 19. Evolution of micropore fraction ψ within the clay layer.

The derivatives with respect to $x_5 = \bar{p}_c$ are of the form (for $A = 1, 2, 3$)

$$A_{A5} = \Delta\lambda \frac{\partial^2 F}{\partial \bar{\epsilon}_A \partial \bar{p}_c}, \quad A_{45} = \frac{\partial F}{\partial \bar{p}_c}, \quad A_{55} = 1, \quad A_{65} = 0. \quad (105)$$

Finally, the derivatives with respect to $x_6 = \psi$ are of the form (for $A = 1, 2, 3, 4$)

$$A_{A6} = 0, \quad A_{56} = -\psi \frac{\partial p_{cm}}{\partial \psi} - p_{cm} - (1 - \psi) \frac{\partial p_{cM}}{\partial \psi} + p_{cM},$$

$$A_{66} = \frac{\partial p_{cm}}{\partial \psi} - \frac{\partial p_{cM}}{\partial \psi}. \quad (106)$$

We note from the chain rule that

$$\frac{\partial p_{cM}}{\partial \psi} = \frac{\partial p_{cM}}{\partial e_M} \frac{\partial e_M}{\partial \psi}, \quad \frac{\partial p_{cm}}{\partial \psi} = \frac{\partial p_{cm}}{\partial v_m} \frac{\partial v_m}{\partial \psi}. \quad (107)$$

Appendix B. Global tangent operator

This appendix develops the elements of the matrix $\mathbf{D} := \partial \mathbf{r} / \partial \mathbf{z}$ necessary for constructing the global tangent operator. The components are $D_{AB} = \partial r_A / \partial z_B$, where the ranges are $A \in [1, 6]$ and $B \in [1, 5]$. For $A, B = 1, 2, 3$,

we have

$$\begin{aligned} D_{AB} &= -\delta_{AB}, & D_{4B} &= 0, \\ D_{5B} &= -\psi \frac{\partial p_{cm}}{\partial \varepsilon_B^{e\text{tr}}} - (1 - \psi) \frac{\partial p_{cM}}{\partial \varepsilon_B^{e\text{tr}}}, \\ D_{6B} &= \frac{\partial p_{cm}}{\partial \varepsilon_B^{e\text{tr}}} - \frac{\partial p_{cM}}{\partial \varepsilon_B^{e\text{tr}}}. \end{aligned} \quad (108)$$

Continuing, we evaluate

$$D_{A4} = D_{A5} = 0, \quad \text{for } A = 1, \dots, 5, \quad D_{64} = 1, \quad D_{65} = -1. \quad (109)$$

References

- [1] M. Al-Mukhtar, 1995, Macroscopic behavior and microstructural properties of a kaolinite clay under controlled mechanical and hydraulic state, in: 1st International Conference on Unsaturated Soils / UNSAT 95, vol. 1, Paris, pp. 3–9.
- [2] P. Delage, M. Audiguier, Y.-J. Cui, M.D. Howat, Microstructure of compacted silt, *Can. Geotech. J.* 33 (1996) 150–158.
- [3] A.K. Didwania, Micromechanical basis of concept of effective stress, *J. Eng. Mech.* 128 (2002) 864–868.
- [4] A. Gens, L.N. Guimarães, M. Sánchez, B. Valleján, Coupled analysis of double porosity swelling clays, in: R.I. Borja (Ed.), *Multiscale and Multiphysics Processes in Geomechanics*, Springer-Verlag, 2011, pp. 85–88.
- [5] A. Mehrabian, Y.N. Abousleiman, Gassmann equations the constitutive relations for multiple-porosity and multiple-permeability poroelasticity with applications to oil and gas shale, *Int. J. Numer. Anal. Methods Geomech.* 39 (2015) 1547–1569.
- [6] Y.N. Abousleiman, S.K. Hoang, C. Liu, Anisotropic porothermoelastic solution and hydro-thermal effects on fracture width in hydraulic fracturing, *Int. J. Numer. Anal. Methods Geomech.* 38 (2014) 493–517.
- [7] K.C. Bennett, L.A. Berla, W.D. Nix, R.I. Borja, Instrumented nanoindentation and 3D mechanistic modeling of a shale at multiple scales, *Acta Geotech.* 10 (2015) 1–14.
- [8] A. Pouya, A finite element method for modeling coupled flow and deformation in porous fractured media, *Int. J. Numer. Anal. Methods Geomech.* 39 (2015) 1836–1852.
- [9] J.R. Silvestre, E. Vargas Jr., L.E. Vaz, A.C. Soares, Modelling of coupled fluid-mechanical problems in fractured geological media using enriched finite elements, *Int. J. Numer. Anal. Methods Geomech.* 39 (2015) 1104–1140.
- [10] S.J. Semmani, J.A. White, R.I. Borja, Thermoplasticity and strain localization in transversely isotropic materials based on anisotropic critical state plasticity, *Int. J. Numer. Anal. Methods Geomech.* (2016) <http://dx.doi.org/10.1002/nag.2536>.
- [11] M. Tjioe, R.I. Borja, On the pore-scale mechanisms leading to brittle and ductile deformation behavior of crystalline rocks, *Int. J. Numer. Anal. Methods Geomech.* 39 (2015) 1165–1187.
- [12] L. Wang, A. Pouya, M. Bornert, B. Halphen, Modelling the internal stress field in argillaceous rocks under humidification/desiccation, *Int. J. Numer. Anal. Methods Geomech.* 38 (2014) 1664–1682.
- [13] M.-N. Vu, A. Pouya, D.M. Seyedi, Theoretical and numerical study of the steady-state flow through finite fractured porous media, *Int. J. Numer. Anal. Methods Geomech.* 38 (2014) 221–235.
- [14] C. Zhu, C. Arson, A thermo-mechanical damage model for rock stiffness during anisotropic crack opening and closure, *Acta Geotech.* 9 (2014) 847–867.
- [15] M. Tjioe, R.I. Borja, Pore-scale modeling of deformation and shear band bifurcation in porous crystalline rocks, *Internat. J. Numer. Methods Engrg.* (2016) <http://dx.doi.org/10.1002/nme.5208>.
- [16] M. Behnia, K. Goshtasbi, M.F. Marji, A. Golshani, Numerical simulation of interaction between hydraulic and natural fractures in discontinuous media, *Acta Geotech.* 10 (2015) 533–546.
- [17] G. Della Vecchia, A.-C. Dieudonné, C. Jommi, R. Charlier, Accounting for evolving pore size distribution in water retention models for compacted clays, *Int. J. Numer. Anal. Methods Geomech.* 39 (2014) 702–723.
- [18] N.-A. Do, D. Dias, P. Oreste, I. Djeran-Maigre, Three-dimensional numerical simulation for mechanized tunnelling in soft ground: the influence of the joint pattern, *Acta Geotech.* 9 (2014) 673–694.
- [19] X.S. Shi, I. Herle, Analysis of the compression behavior of artificial lumpy composite materials, *Int. J. Numer. Anal. Methods Geomech.* (2016) <http://dx.doi.org/10.1002/nag.2493>.
- [20] X.S. Shi, I. Herle, Numerical simulation of lumpy soils using a hypoplastic model, *Acta Geotech.* (2016) <http://dx.doi.org/10.1007/s11440-016-0447-7>.
- [21] K.-H. Xie, C.-Q. Xia, R. An, H.-W. Ying, H. Wu, A study on one-dimensional consolidation of layered structured soils, *Int. J. Numer. Anal. Methods Geomech.* 40 (2016) 1081–1098.
- [22] D.S. Park, B. Kutter, Sensitive bounding surface constitutive model for structured clay, *Int. J. Numer. Anal. Methods Geomech.* (2016) <http://dx.doi.org/10.1002/nag.2507>.
- [23] W. Shen, Z. He, L. Dormieux, D. Kondo, Effective strength of saturated double porous media with a Drucker–Prager solid phase, *Int. J. Numer. Anal. Methods Geomech.* 38 (2014) 281–296.
- [24] A. Koliji, L. Laloui, O. Cusinier, L. Vulliet, Suction induced effects on the fabric of a structured soil, *Transp. Porous Media* 64 (2006) 261–278.
- [25] A. Koliji, L. Laloui, L. Vulliet, Constitutive modeling of unsaturated aggregated soils, *Int. J. Numer. Anal. Methods Geomech.* 34 (2010) 1846–1876.

- [26] A. Koliji, L. Vulliet, L. Laloui, Structural characterization of unsaturated aggregated soil, *Can. Geotech. J.* 47 (2010) 297–311.
- [27] M.D. Liu, J.P. Carter, A structured Cam Clay model, *Can. Geotech. J.* 39 (2002) 1313–1332.
- [28] M. Kavvas, A. Amorosi, A constitutive model for structured soils, *Géotechnique* 50 (2000) 263–273.
- [29] A. Koliji, P. Lehmann, L. Vulliet, L. Laloui, A. Carminati, P. Vontobel, R. Hassanein, Assessment of structural evolution of aggregated soil using neutron tomography, *Water Resour. Res.* 44 (2009) W00C07. <http://dx.doi.org/10.1029/2007WR006297>.
- [30] A. Koliji, Mechanical behaviour of unsaturated aggregated soils, (Ph.D. thesis), Ecole Polytechnique Fédérale de Lausanne, 2008, No. 4011.
- [31] A. Koliji, L. Vulliet, L. Laloui, New basis for the constitutive modelling of aggregated soils, *Acta Geotech.* 3 (2008) 61–69.
- [32] G. Barrenblatt, I. Zheltov, I. Kochina, Basic concepts in the theory of seepage of homogeneous liquids in fissured rocks, *J. Appl. Math. Mech.* 24 (1960) 1286–1303.
- [33] G. Barrenblatt, On certain boundary value problems for the equation of seepage of liquid in fissured rock, *J. Appl. Math. Mech.* 27 (1963) 513–518.
- [34] N. Khalili, S. Valliappan, Unified theory of flow and deformation in double porous media, *Eur. J. Mech. A Solids* 15 (1996) 321–336.
- [35] C. Callari, F. Federico, FEM validation of a double porosity elastic model for consolidation of structurally complex clayey soils, *Int. J. Numer. Anal. Methods Geomech.* 24 (2000) 367–402.
- [36] W.K.S. Pao, R.W. Lewis, Three-dimensional finite element simulation of three phase flow in a deforming fissured reservoir, *Comput. Methods Appl. Mech. Engrg.* 191 (2002) 2631–2659.
- [37] N. Khalili, R. Witt, L. Laloui, L. Vulliet, A. Koliji, Effective stress in double porous media with two immiscible fluids, *Geophys. Res. Lett.* 32 (L15309) (2005) <http://dx.doi.org/10.1029/2005GL023766>.
- [38] K. Hutter, L. Laloui, L. Vulliet, Thermodynamically based mixture models of saturated and unsaturated soils, *Mech. Cohesive-frictional Mater.* 4 (1999) 295–338.
- [39] S.M. Hassanizadeh, W.G. Gray, Mechanics and thermodynamics of multiphase flow in porous-media including interphase boundaries, *Adv. Water Resour.* 13 (1990) 169–186.
- [40] W.G. Gray, B.A. Schrefler, Thermodynamic approach to effective stress in partially saturated porous media, *Eur. J. Mech. A Solids* 20 (2001) 521–538.
- [41] W.G. Gray, B.A. Schrefler, Analysis of the solid phase stress tensor in multiphase porous media, *Int. J. Numer. Anal. Methods Geomech.* 31 (2007) 541–581.
- [42] R.I. Borja, Cam-Clay plasticity, Part V: A mathematical framework for three-phase deformation and strain localization analyses of partially saturated porous media, *Comput. Methods Appl. Mech. Engrg.* 193 (2004) 5301–5338.
- [43] R.I. Borja, On the mechanical energy and effective stress in saturated and unsaturated porous continua, *Int. J. Solids Struct.* 43 (2006) 1764–1786.
- [44] G.T. Houlsby, The work input to a granular material, *Géotechnique* 29 (1979) 354–358.
- [45] G.T. Houlsby, The work input to an unsaturated granular material, *Géotechnique* 47 (1997) 193–196.
- [46] R.I. Borja, A. Koliji, On the effective stress in unsaturated porous continua with double porosity, *J. Mech. Phys. Solids* 57 (2009) 1182–1193.
- [47] H.H. Gerke, Preferential flow descriptions for structured soils, *J. Plant Nutrition Soil Sci.* 169 (2006) 382–400.
- [48] J. Šimůnek, N.J. Jarvis, M.T. van Genuchten, A. Gardenas, Review and comparison of models for describing non-equilibrium and preferential flow and transport in the vadose zone, *J. Hydrol.* 272 (2003) 14–35.
- [49] A. Carminati, A. Kaestner, P. Lehmann, H. Flüher, Unsaturated water flow across soil aggregate contacts, *Adv. Water Resour.* 31 (2008) 1221–1232.
- [50] J.B. Burland, On the compressibility and shear strength of natural clays, *Géotechnique* 40 (1990) 329–378.
- [51] A.G. Anagnostopoulos, N. Kalteziotis, G.K. Tsiambaos, Kavvas, Geotechnical properties of the Corinth Canal marls, *Geotech. Geol. Eng.* 9 (1991) 1–26.
- [52] E.E. Alonso, A. Gens, A. Josa, A constitutive model for partially saturated soils, *Géotechnique* 40 (1990) 405–430.
- [53] J. Choo, J.A. White, R.I. Borja, Hydromechanical modeling of unsaturated flow in double porosity media, *Int. J. Geomech.* (2016) [http://dx.doi.org/10.1061/\(ASCE\)GM.1943-5622.0000558](http://dx.doi.org/10.1061/(ASCE)GM.1943-5622.0000558).
- [54] R. Butterfield, A natural compression law for soils, *Géotechnique* 29 (1979) 469–480.
- [55] R.I. Borja, *Plasticity Modeling and Computation*, Springer-Verlag, Berlin, Heidelberg, 2013.
- [56] R.I. Borja, E. Alarcón, A mathematical framework for finite strain elastoplastic consolidation Part 1: Balance laws, variational formulation, and linearization, *Comput. Methods Appl. Mech. Engrg.* 122 (1995) 145–171.
- [57] R.I. Borja, C. Tamagnini, E. Alarcón, Elastoplastic consolidation at finite strain part 2: finite element implementation and numerical examples, *Comput. Methods Appl. Mech. Engrg.* 1259 (1998) 103–122.
- [58] N. Benkemoun, R. Gelet, E. Roubin, J.-B. Colliat, Poroelastic two-phase material modeling: theoretical formulation and embedded finite element method implementation, *Int. J. Numer. Anal. Methods Geomech.* 39 (2015) 1255–1275.
- [59] J. Choo, R.I. Borja, Stabilized mixed finite elements for deformable porous media with double porosity, *Comput. Methods Appl. Mech. Engrg.* 293 (2015) 131–154.
- [60] K. Wang, W. Sun, A semi-implicit discrete-continuum coupling method for porous media based on the effective stress principle at finite strain, *Comput. Methods Appl. Mech. Engrg.* 304 (2016) 546–583.
- [61] M. Goudarzi, S. Mohammadi, Weak discontinuity in porous media: an enriched EFG method for fully coupled layered porous media, *Int. J. Numer. Anal. Methods Geomech.* 38 (2014) 1792–1822.
- [62] N. Guo, J. Zhao, Parallel hierarchical multiscale modelling of hydro-mechanical problems for saturated granular soil, *Comput. Methods Appl. Mech. Engrg.* 305 (2016) 37–61.
- [63] J.A. White, N. Castelletto, H.A. Tchelepi, Block-partitioned solvers for coupled poromechanics: A unified framework, *Comput. Methods Appl. Mech. Engrg.* 303 (2016) 55–74.
- [64] E.W. Remij, J.J.C. Remmers, J.M. Huyghe, D.M.J. Smeulders, The enhanced local pressure model for the accurate analysis of fluid pressure driven fracture in porous materials, *Comput. Methods Appl. Mech. Engrg.* 286 (2015) 293–312.

- [65] G. Meschke, D. Leonhart, A Generalized Finite Element Method for hydro-mechanically coupled analysis of hydraulic fracturing problems using space–time variant enrichment functions, *Comput. Methods Appl. Mech. Engrg.* 290 (2015) 438–465.
- [66] W. Sun, Q. Chen, J.T. Ostien, Modeling the hydro-mechanical responses of strip and circular punch loadings on water-saturated collapsible geomaterials, *Acta Geotech.* 9 (2014) 903–934.
- [67] W. Sun, A stabilized finite element formulation for monolithic thermo-hydro-mechanical simulations at finite strain, *Internat. J. Numer. Methods Engrg.* 103 (2015) 798–839.
- [68] X. Song, R.I. Borja, Mathematical framework for unsaturated flow in the finite deformation range, *Internat. J. Numer. Methods Engrg.* 14 (2014) 658–682.
- [69] X. Song, R.I. Borja, Finite deformation and fluid flow in unsaturated soils with random heterogeneity, *Vadose Zone J.* 13 (2014) <http://dx.doi.org/10.2136/vzj2013.07.0131>.
- [70] J. Bear, *Dynamics of Fluids in Porous Media*, Dover Publications, Inc., New York, 1972.
- [71] J. Warren, P. Root, The behavior of naturally fractured reservoirs, *SPE J.* 3 (1963) 245–255.
- [72] R.C. Dykhuizen, A new coupling term for dual-porosity models, *Water Resour. Res.* 26 (1990) 351–356.
- [73] H.H. Gerke, M.T. van Genuchten, A dual-porosity model for simulating the preferential movement of water and solutes in structured porous media, *Water Resour. Res.* 29 (1993) 305–319.
- [74] R. Haggerty, S.M. Gorelick, Multiple-rate mass transfer for modeling diffusion and surface reactions in media with pore-scale heterogeneity, *Water Resour. Res.* 31 (1995) 2383–2400.
- [75] J.M. Köhne, B.P. Mohanty, J. Šimůnek, H.H. Gerke, Numerical evaluation of a second-order water transfer term for variably saturated dual-permeability models, *Water Resour. Res.* 40 (2004) W07409.
- [76] P. Sarma, K. Aziz, New transfer functions for simulation of naturally fractured reservoirs with dual porosity models, *SPE J.* 11 (2006) 328–340.
- [77] N. Trottier, F. Delay, O. Bildstein, P. Ackerer, Inversion of a dual-continuum approach to flow in a karstified limestone: insight into aquifer heterogeneity revealed by well-test interferences, *J. Hydrol.* 508 (2014) 157–169.
- [78] J.H. Argyris, G. Faust, J. Szimmat, E.P. Warnke, K.J. Willam, Recent developments in the finite element analysis of prestressed concrete reactor vessels, *Nucl. Eng. Des.* 28 (1974) 42–75.
- [79] G. Gudehus, Elastoplastische Stoffgleichungen für trockenen Sand, *Ingenieur-Archiv.* 42 (1973) 151–169.
- [80] V. Navarro, E.E. Alonso, Secondary compression of clays as a local dehydration process, *Géotechnique* 51 (2001) 859–869.
- [81] M. Murad, J.N. Guerreiro, A.F.D. Loula, Micromechanical computational modeling of secondary consolidation and hereditary creep in soils, *Comput. Methods Appl. Mech. Engrg.* 190 (2001) 1985–2016.
- [82] P. Cosenza, D. Korošak, Secondary consolidation of clay as an anomalous diffusion process, *Int. J. Numer. Anal. Methods Geomech.* 38 (2014) 1231–1246.
- [83] L. Callisto, G. Calabresi, Mechanical behaviour of a natural soft clay, *Géotechnique* 48 (1998) 495–513.